




Isaac Hinz

Simulated Diagenesis of the Iron-Silica Precipitates in Banded Iron Formations

submitted in partial fulfillment of the requirements for the degree of
Master of Science in Earth and Environmental Sciences
Department of Earth and Environmental Sciences
The University of Michigan

 Signature	Accepted by:	
	Jena E. Johnson	5/19/2022
	Name	Date
	Jie Li	05/28/2022
Signature	Name	Date
	Marin K. Clark	6/28/2022
Department Chair Signature	Name	Date

I hereby grant the University of Michigan, its heirs and assigns, the non-exclusive right to reproduce and distribute single copies of my thesis, in whole or in part, in any format. I represent and warrant to the University of Michigan that the thesis is an original work, does not infringe or violate any rights of others, and that I make these grants as the sole owner of the rights to my thesis. I understand that I will not receive royalties for any reproduction of this thesis.

- Permission granted.
- Permission granted to copy after: _____
- Permission declined.


Author Signature



Simulated Diagenesis of the Iron-Silica Precipitates in Banded Iron Formations

Isaac L. Hinz

University of Michigan

Abstract

Banded Iron Formations, or BIFs, are chemically precipitated sediments that record Archean ocean geochemistry. BIFs are laminated silica- and iron-rich deposits that host a range of iron(II, III) minerals, including hematite, magnetite, siderite, greenalite, minnesotaite, and stilpnomelane. This diverse mineralogical assemblage reflects secondary mineralization reactions due to diagenesis and/or post-depositional alteration. While petrographic observations of BIFs sparingly contain the iron silicate greenalite, recent evidence of greenalite nanoparticles preserved in early-mineralizing BIF chert suggest greenalite was a primary mineral in BIF progenitor sediments. Therefore, investigating the precipitation mechanism(s) of greenalite and how diagenesis impacts iron silicate formation and transformation would further constrain the Archean ocean environment and help unravel post-depositional processes. To examine how iron silicates crystallize and/or transform with increased temperatures, we simulated the diagenesis of iron silicates. We first precipitated a Fe-rich proto serpentine under Archean ocean conditions at neutral pH by performing in situ Fe(II) oxidation experiments at 25 °C in the presence of silica. Subjected to simulated diagenesis at 80 °C, the Fe-rich proto phyllosilicates were then transformed into a crystalline phyllosilicate characterized as 30% cronstedtite-70% greenalite accompanied by magnetite. At temperatures ≥ 150 °C, we continued to observe increased magnetite formation that coincided with the loss of iron and elevated incorporation of Mg into the phyllosilicate as it further recrystallized into Mg-greenalite. Our findings demonstrate a possible formation mechanism of early silicates through partial Fe(II) oxidation and support petrographic observations that magnetite can be derived from the diagenesis of iron phyllosilicates. Additionally, we suggest that Mg contents in BIF iron phyllosilicates could serve as a tracer for diagenesis, with Mg signaling phyllosilicate-fluid interactions at elevated temperatures. Ultimately, our experiments help reveal how initial iron phyllosilicate precipitates are altered during diagenesis, providing novel insights into the interpretation of greenalite and magnetite in ancient BIF assemblages.

Keywords: greenalite, crystallization, magnesium substitution, magnetite, serpentine

Introduction

Chemical sediments provide an archive of (bio)geochemical processes. The oceans on Archean [4.0-2.5 billion years ago, Ga] Earth were actively precipitating and depositing authigenic (formed in place on the seafloor) chemical sediments, which therefore can serve a proxy for the ancient marine (bio)geochemistry and signals of the evolution of life (Derry and Jacobson 1990). A prominent example of such sediments are the banded iron formation (BIF) deposits, laminated sedimentary deposits that contain at least 15% iron and commonly also host a high silica content (James 1954). BIFs provide the best record of ancient marine conditions in the Archean ocean, with their chemistry interpreted as reflecting an iron and silica rich system (Klein 2005; Bekker et al. 2014).

The presence of BIF deposits in ancient oceans require a mechanism to initially induce chemical precipitation (Holland 1984). Minerals recorded in BIFs contain Fe(II) and Fe(III) with an average oxidation state of $\text{Fe}^{2.4+}$ (Klein and Beukes 1992). This is indicative of a partially oxidative environment, the result of biotic and/or abiotic process(es) in Archean oceans and sediments. Extensive BIF deposition occurred in the Archean Eon, which had little to no molecular oxygen until the Great Oxygenation Event at ~ 2.3 Ga (Gumsley et al. 2017; Farquhar et al. 2011; Poulton et al. 2021; Johnson and Molnar 2019). Estimates place atmospheric O_2 prior to this rise in oxygen as < 1 ppm or less than $\sim 10^{-5.7}$ atmosphere (atm) (Pavlov and Kasting 2002; Farquhar et al. 2011). An early, and still popular, hypothesis for the deposition of precursor BIF sediments invoked low levels of dissolved O_2 in the ocean reacting with dissolved Fe^{2+} to consume marine oxygen and form insoluble Fe^{3+} precipitates such as ferric (oxyhydr)oxides (Cloud 1973; Bekker et al. 2014; Konhauser et al. 2017). Others have attributed the chemical sedimentation of BIF progenitor precipitates to the products of anoxygenic Fe^{2+} -oxidizing photosynthesis (Hartman 1984; Kappler et al. 2005; Konhauser et al. 2002) or reactions between Fe^{2+} and ultraviolet light (Cairns-Smith 1978; Braterman et al. 1983; Bekker et al. 2010).

To identify the potential processes responsible for their formation, the iron-rich muds and cherts in BIFs have been intensely investigated. However, the primary BIF sediments experienced physical and chemical alteration as they transformed into sedimentary rock through the process of diagenesis, and most of these rocks were then subject to subsequent post depositional alteration, fluid flow, and metamorphism (Beukes 1984; Fischer and Knoll 2009; Trendall 2002). Consequently, none of the minerals in BIFs are considered primary and modern-day BIF deposits are composed of a disequilibrium mixture of hematite, magnetite, iron-rich carbonates, iron silicates, and chert minerals (Klein 2005; Bekker et al. 2014; Konhauser et al. 2017). This complexity has led to an ongoing debate to determine the initial mineral(s) associated with BIFs, as only the original precipitates would accurately reflect Archean marine geochemistry and potentially biology.

The effects of diagenesis and later alteration complicates the detection of the initial amorphous and/or metastable phases precipitated in Archean oceans, and competing hypotheses suggest two different original BIF precipitates. Earlier models, supplemented by numerous observations of BIFs, pointed to ferric oxides or hydroxides being the primary iron precipitate (James 1954; Cloud 1973; Klein and Beukes 1989; Beukes and Gutzmer 2008; Sun et al. 2015). However, recent studies examined early-mineralizing chert within BIFs that can serve as a barrier to diagenesis, preserving microbial fossils and the early assemblage of minerals. These

investigations discovered inclusions of iron-rich silicate nanoparticles and suggested these iron silicates were primary minerals from the Archean ocean (Muhling and Rasmussen 2021; Rasmussen et al. 2015; Rasmussen et al. 2019). Further characterization of the iron silicate nanoparticles concluded they contained < 0.5 atomic% (at.%) to undetectable quantities of magnesium and ~10-25% Fe(III) (Johnson et al. 2018; Rasmussen et al. 2018), placing them within the solid solution space between greenalite $[(\text{Fe}^{2+}, \text{Mg})_3\text{Si}_2\text{O}_5(\text{OH})_4]$ and cronstedtite $[(\text{Fe}^{2+}, \text{Fe}^{3+}, \text{Mg})_3(\text{Si}, \text{Fe}^{3+})_2\text{O}_5(\text{OH})_4]$, serpentine group iron silicates with 7 Ångstrom (Å) lattice spacing.

These recent observations call for an understanding of the geochemical conditions and mechanism(s) required to form iron silicates under plausible Archean ocean conditions. Previous anoxic experiments conducted at low temperatures of 20-25 °C reported the formation of amorphous to poorly crystalline iron(II)-silica precipitates, proposed to be proto-silicates, when pH was ≥ 7.5 (Farmer et al. 1991; Tosca et al. 2016). The analyses performed on these iron-silica precipitates could not definitively conclude whether these precipitates were a heterogeneous mix of Fe(II) and Si-rich phases or homogenous Fe(II)-silicates (Francisco 2020). However, similar experiments in another study demonstrated that the initial Fe(II)-Si coprecipitates at pH 7.5 could be hydrothermally aged into greenalite-like phases with ~7 Å lattice spacing (Hinz et al. 2021). Yet another concern with the relevance of these experiments is that the pH of ≥ 7.5 used in these experiments was higher than the hypothesized pH of the Archean ocean, which was constrained to pH ~6.5-7.0 by two independent marine and atmospheric geochemical models (Halevy and Bachan 2017; Krissansen-Totten et al. 2018) and considerations of authigenic clay formation (Isson and Planavsky 2018). An additional issue with Fe(II)-silicate precipitation generating the initial BIF sediments is that this Fe(II)-silica saturation mechanism would not account for the low levels of Fe(III) detected in the BIF iron silicate inclusions.

To address whether ferric iron can in fact induce precipitation of iron silicates at lower pH, we previously examined the precipitate products resulting from the addition of low amounts of aqueous (aq) Fe(III) to ferrous iron- and silica-rich conditions at a more plausible Archean ocean pH of 6.5-7.0 (Hinz et al. 2021). We found that Fe(III) (aq) triggered the low-temperature precipitation of an amorphous iron and silica-rich phase accompanied by rare layered silicate-like structures at these more relevant pH values. Earlier studies have simulated diagenesis by hydrothermally aging iron and/or magnesium and silica suspensions at ≥ 60 °C to promote the crystallization of silicates (Baldermann 2014; Mizutani et al. 1991; Tosca et al. 2011). When we hydrothermally aged our Fe(II,III)-silica precipitates at 150 °C, we identified the crystalline products as ~7 Å iron phyllosilicates, similar to BIF greenalite but more magnesium-rich, along with additional green rust carbonate, magnetite, hematite, and magnesite (Hinz et al. 2021).

The heterogeneous assemblage that we observed after Fe(III) (aq) additions and 150 °C aging treatment motivated us to explore an alternative precipitation mechanism and hydrothermal aging scheme at several temperatures. In this study, we instigated in situ partial Fe(II) oxidation at pH 7 in the presence of silica by bubbling low concentrations of oxygen gas into simulated Archean ocean conditions. The initial partially-oxidized iron-silica precipitates that formed at room temperature (25 °C) were plausible analogues for ambient Archean water column phase(s). We progressively hydrothermally aged these precipitates to promote crystallization and simulate chemical reactions over the typical diagenetic temperature interval up to 200 °C (Brenner et al. 1991; Siever 1986). Based on previous experimental studies of

silicate systems, we hydrothermally aged at our initial iron-silica precipitates in sequential steps at 80 °C (Pignatelli et al. 2013; Vachner et al. 2019), 150 °C (Baldermann et al. 2014; Mizutani et al. 1991) and 220 °C (Janecky and Seyfried 1986) within anoxic, sealed vessels to mimic varying levels of diagenesis and compared these precipitates to low-temperature (25 °C) products. Over the course of the simulated diagenesis, we measured solution chemistry and characterized the resultant precipitates as they crystallized and transformed.

Methods

Experimental Solution Setup

All experiments originated from bulk uniform solutions prepared in 4 L wide mouth jugs at room temperature with 18.2 M Ω -cm ultrapure water. The ultrapure water used was boiled before being covered with aluminum foil and purged with pure N₂ gas to deoxygenate the water. Next, the water was brought into a MBraun glovebox consisting of an N₂ atmosphere (< 0.1 ppm O₂) where it was stirred uncapped for at least 72 hours to release any residual oxygen in solution. All solid chemical reagents were weighed outside the glovebox before being transported into the glovebox to be dissolved in deoxygenated water used in experimentation.

We prepared a 3.6 L solution in duplicate where first sodium orthosilicate (Na₄SiO₄) was dissolved in the aforementioned anoxic ultrapure water to a final concentration of 1.1 mM Si. Estimated dissolved silica in Archean seawater was expected to be between ~0.67 mM to an upper limit at amorphous SiO₂ saturation of, ~1.9 mM (Siever 1992; Maliva et al. 2005; Stefurak et al. 2015; Gunnarsson and Arnórsson 2000); we therefore chose an intermediate level between these constraints and below amorphous silica precipitation. The solution was stirred and the pH was measured with a ThermoFisher Orion Star A221 pH meter while being adjusted to pH 7 by dropwise additions of 1 M hydrochloric acid (HCl). The solution was continuously stirred in the glovebox for 24 hours to allow for the depolymerization of the dissolved silica in solution (Dietzel 2000). Next, the pH was momentarily adjusted to 3 before we added salts expected for the Archean ocean (Table 1) until they were fully dissolved.

Chemical Component, Chemical Formula	Concentration [mM]
Sodium chloride, NaCl	400
Sodium bicarbonate, NaHCO ₃	30

Magnesium chloride hexahydrate, $\text{MgCl}_2 \cdot 6\text{H}_2\text{O}$ *	10
Ammonium chloride, NH_4Cl	10
Potassium chloride, KCl	7
Sodium orthosilicate, Na_4SiO_4	$1.1 \pm 0.08^*$
Ferrous chloride tetrahydrate, $\text{FeCl}_2 \cdot 4\text{H}_2\text{O}$	$1.1 \pm 0.09^*$

Table 1. Composition of recreated Archean seawater. Iron and silica concentrations shown as measured concentrations derived from colorimetric (ferrozine and silicomolybdate) assays where * denotes the standard deviation of the measurement.

Assuming constant salinity over time, our Archean solution had 400 mM sodium chloride and 7 mM potassium chloride (Table 1) as observed in modern ocean systems (Riley and Chester 1971). Archean ocean models have estimated ammonium to be 0.03-10 mM (Stüeken 2016), and therefore we added 10 mM ammonium chloride at the upper end of this range to help ensure reducing conditions were maintained (Table 1). The magnesium content in Archean oceans have been estimated to be 10-30 mM (Jones et al. 2015), with processes associated with hydrothermal seawater-oceanic crust interactions decreasing dissolved magnesium in ocean water from today's concentration of ~50 mM (Spencer and Hardie 1990; Halevy and Bachan 2017; Izawa et al. 2010). Thus we used the lower estimate and added 10 mM magnesium chloride (Table 1). The maximum concentration of ferrous iron, ~2 mM in Archean oceans, has been suggested to be set by the supersaturation of the ferrous silicates (Jiang and Tosca 2019) or Fe(II) phosphates (Derry 2015). Therefore, we set Fe(II) to 1.1 mM using a 300 mM ferrous chloride tetrahydrate stock, adding at pH 3 to avoid pH-driven precipitation of Fe(II) phases.

The pH was then readjusted to ~5 with 1 M sodium hydroxide (NaOH) to limit the exsolution of CO_2 (aq) at $\text{pH} < 5$ before the addition of our sodium bicarbonate buffer. Archean oceans have been estimated to contain 5-30 mM bicarbonate (Blättler et al. 2017). Additionally, the presence of common organic buffers (HEPES & MOPS) have been shown to impact iron oxidation (Buchholz et al. 2011). Therefore we added the highest estimate for bicarbonate, 30 mM (Table 1), to maximize inorganic buffering. The bicarbonate buffer was added to the solution dropwise, gradually increasing the solution pH until around pH 6.7-6.9 where it was held by 1 M HCl and 1 M NaOH additions to keep the $\text{pH} \leq 7$. After the bicarbonate buffer was added, the solution was readjusted back to pH 7 at 15 minute intervals for 2 hours, as the solution

had the tendency to drift to pH 7.2-7.3 over time. The stir bar was removed from the bottle to limit nucleation. The duplicate 3.6 L solutions were gently mixed together three times in 4 L jugs to create one homogeneous bulk solution (total 7.2 L) that was measured to have a pH of 7.0 prior to experimentation.

The bulk solution was then transferred as 510 mL portions to 610 mL borosilicate glass bottles. Each bottle was outfitted with a 1.5 mm chemically resistant silicone rubber seal nested in a Restek™ GL-45 Mobi-Cap with two ¼"-28 threaded ports (Restek™#27835). The bottles were then wrapped in aluminum foil to prevent any possible ultraviolet (UV) photooxidation of Fe(II). Six of the newly sealed experiments were laid on their side and remained in the glovebox to act as ferrous controls. The remaining six identical bottles were removed from the glovebox to be bubbled with low O₂.

Low O₂ Bubbling

To partially oxidize the Fe(II) (aq) in situ under simulated Archean ocean conditions, six sealed experimental bottles were transported to a multi-valve gassing station. Two ¼" -28 threaded screws were removed to expose a small portion of the silicone rubber seal. We next connected a 4" needle to the multi-valve gassing station to provide N₂ mixed with 49.1 ± 0.9 ppm O₂, puncturing through the silicone rubber seal in port 1 to bubble gas into the solution. Then, a separate 2" needle was quickly punctured through port 2 of the silicone rubber seal to allow for gas exchange and pressure relief of the system. Each solution was continuously bubbled at 3 psi at 25 °C for 90 minutes.

Solution samples from each experiment were extracted at 15 minute intervals, the pH was measured on a ThermoFisher Orion Star A221 pH meter, and the values were recorded in Table 2. With every 15 minutes of bubbling, the pH of the system increased by an average of 0.09 units, likely due to the exsolution of CO₂(aq)/H₂CO₃*. To mitigate this effect, anoxic 2 M HCl was added in dropwise to readjust the pH back to 7 during O₂ bubbling.

Bubbling Experiment	1	2	3	4	5
pH after 15 minutes	7.04	7.11	7.14	7.05	7.1
pH after 30 minutes	7.11	7.12	7.08	7.08	7.09
pH after 45 minutes	6.92	6.96	7	7.09	7.08
pH after 60 minutes	6.98	6.91	7.02	6.92	6.97

pH after 75 minutes	6.99	6.97	6.98	7.05	7.07
pH after 90 minutes	7.02	7.01	6.99	7.03	6.98

Table 2: Measured pH for each experiment during the O₂ bubbling process at 25 °C where solutions were adjusted by anoxic 2 M hydrochloric acid to hold the pH around 7. Note: the error for each pH measurement was ± 0.02 pH units.

After 90 minutes, the 2" pressure relief needle was removed, quickly sealed with the screw followed by the 4" gassing needle being removed and sealed with a screw to lock in the headspace. The upright bottle was then tilted 90° to maximize the headspace-solution contact and limit any unwanted interaction of O₂ from the surrounding environment. The tilted bottles were transported back into the glovebox and remained resting on their side wrapped in aluminum foil.

Initial Fe(II) Oxidation and pH

The bubbled and control experiments were allowed to react and equilibrate horizontally in the glovebox at 25 °C. Each bottle was shaken horizontally three times a week to homogenize the solution. After 19 days, we observed that increases in precipitate quantity had stopped for > 4 days and deemed that the Fe(II) (aq) was allowed to fully react in situ with the added O₂. We then measured the pH of each control and bubbled experiment (Table 3).

Temperature (°C)	Time (Days)	Bubbled (pH)	Control (pH)
25	19	7.33	7.14
25	40	7.06	7.17
80	7 (26)	6.74	6.92
150	7 (33)	6.41	6.43
220	7 (40)	5.85	7.65

Table 3. pH measurements of Parr vessel precipitates and overlaying solution for control and bubbled experiments for temperatures that ranged from 25-220 °C. Note: pH measurements were taken after the solution was cooled to 25 °C to minimize temperature compensation and the error for each pH measurement was ± 0.02 pH units.

To measure the extent of Fe(II) oxidation (reported as Fe(III)/FeT), one of each of the bubbled and control experimental bottles were unsealed and completely acidified with anoxic 4 M HCl to a pH of 3 for > 12 hours, after which all visible precipitate was dissolved. Subsequently, the dissolved experimental solutions were analyzed by the ferrozine assay (Stookey 1970; Viollier et al. 2000) to determine the bulk Fe(III)/FeT (Table 4) after equilibration for 19 days at 25 °C (Fig. 1). In addition, a precipitate subsample from the bubbled experiments after 19 days at 25 °C (Fig. 1) was removed, washed three times between centrifuging, and acidified to complete dissolution before being analyzed by the ferrozine assay (Table 4).

Condition	Measurement	Standard Deviation
Silica in initial solution [mM]	1.1	± 0.08
Fe(II) in initial solution [mM]	1.1	± 0.03
<u>Fe[III]</u> in acidified control solution after 19 days 25° C FeT	0.07	± 0.02
<u>Fe[III]</u> in acidified bubbled solution after 19 days 25° C FeT	0.75	± 0.05
<u>Fe[III]</u> in bubbled solids after 19 days 25° C FeT	0.48	± 0.06

Table 4: Summary of experimental results of Fe(II) and silica in initial solutions. The measured Fe[III]/FeT content for the acidified control and bubbled experiments (solution plus precipitate) after aging in a borosilicate bottle at 25 °C for 19 days.

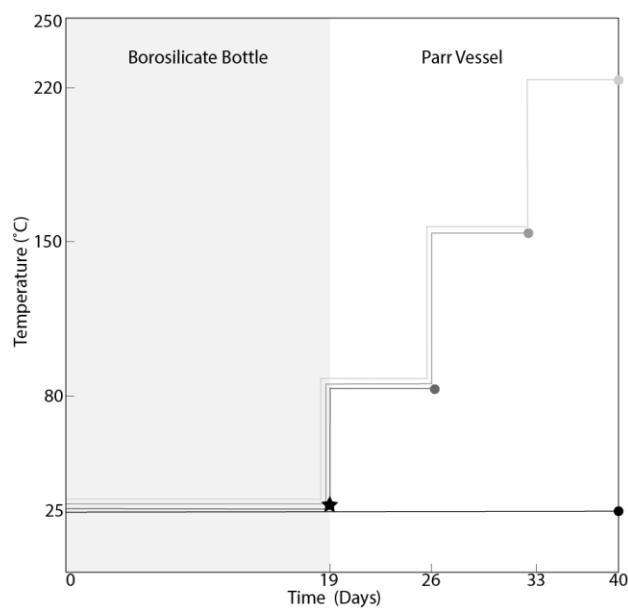


Figure 1: Time-temperature scheme for hydrothermal aging of control and bubbled experiments. The reaction with O₂ and equilibrium period took place in borosilicate bottles denoted by the light gray region. Control and bubbled experiments were subsampled for pH (Table 3) and Fe(III)/FeT (Table 4) after 19 days at room temperature (star symbol). The remainder of material was portioned and transferred into anoxic Parr vessels for aging at 25, 80, 150, and 220 °C before being sampled (filled circles, Table 5).

Hydrothermal Aging and Subsampling

The remaining four control and four bubbled experimental solutions were mixed together to homogenize. The solution, along with any precipitate present, was equally distributed in 15 mL increments into eight separate 22 mL stainless steel gas-tight Parr vessels fit with a PTFE gasket and anoxically sealed. One of each of the control and bubbled experiments remained sealed in a Parr vessel within the glovebox at 25 °C for the duration of simulated diagenesis (total of 40 days). Three control and three bubbled experiments in Parr vessels were taken out of the glovebox and placed into a Thermo Scientific™ Heratherm™ oven set at 80 °C to undergo hydrothermal aging.

After 7 additional days of hydrothermal aging at 80 °C, one of the control and bubbled Parr vessels were removed from the oven and transferred to the glovebox (Fig. 1). The hydrothermally aged 80 °C vessels were allowed to cool to 25 °C before a pH measurement of the solution was taken (Table 3). If a precipitate was present, the precipitate slurry was centrifuged three times and rinsed with anoxic water with a pH \pm 0.1 of the measured value (Table 3) to limit pH-driven reactions after simulated diagenesis while removing excess salts prior to analysis. The precipitate was then subsampled for future analysis and stored in anoxically-sealed Mylar bags within the glovebox at 25 °C. The oven temperature was increased to 150 °C for the remaining Parr vessels.

After 7 additional days at 150 °C, another control and bubbled Parr vessel were withdrawn from the oven and taken to the glovebox (Fig. 1). The experimental solutions were again cooled to 25 °C in the glovebox before the pH was measured (Table 3), and any precipitate was rinsed and apportioned for future analysis. Then, the oven temperature for the remaining two Parr vessels was increased to 220 °C.

After 7 additional days at 220 °C, the last remaining control and bubbled Parr vessels were transferred to the glovebox (Fig. 1). The solution pH was measured (Table 3), and the precipitate was rinsed and allocated for future analysis. The control and bubbled Parr vessels that remained in the glovebox for the entire 40 days at 25 °C were measured for pH (Table 3), and any precipitate was rinsed and subsampled for future analysis. We estimate that the maximum pressure experienced during simulated diagenesis was 0.5 atm at 80 °C, 4.7 atm at 150 °C, and 23 atm at 220 °C, with the ions in solution likely lowering the overall saturation vapor pressure.

Analytical Sample Preparation and Instrument Parameters

Fe(III)/FeT Content of Solids

Control and bubbled experiments that produced precipitates were acidified with anoxic 4 M HCl, vigorously shaken, and allowed to fully dissolve for > 12 hours. Dissolved precipitates were analyzed by the ferrozine assay from three subsamples (Stookey 1970; Viollier et al. 2000) to determine the Fe(III)/FeT content reported in Table 4 and 5.

Condition	Measurement	Standard Deviation
<u>Fe[III]</u> in bubbled solids after 40 days 25° C FeT	0.45	1.8
<u>Fe[III]</u> in bubbled solids after 7 (26) days 80° C FeT	0.45	2.5
<u>Fe[III]</u> in bubbled solids after 7 (33) days 150° C FeT	0.51	0.06
<u>Fe[III]</u> in bubbled solids after 7 (40) days 220° C FeT	0.46	2.4
<u>Fe[III]</u> in control solids after 7 (33) days 150° C FeT	0.27	0.9
<u>Fe[III]</u> in control solids after 7 (40) days 220° C FeT	0.32	2

Table 5. The measured Fe[III]/FeT content of the acidified control and bubbled solid precipitate from conditions ranging 25-220 °C over 19-40 total days.

X-ray Diffraction (XRD)

A precipitate slurry was pipetted as 20 μ L subsamples into Cole-Parmer Kapton tubes with an inner diameter of 1.46 mm and with a 0.05 mm wall thickness. Kapton tubes filled with experimental precipitate were allowed to partially dry for 12 hours in the glovebox before both ends of the Kapton tubes were heat sealed shut. The sealed Kapton tubes were protectively placed in 15 mL falcon tubes and heat sealed in mylar bags prior to shipping. Samples were sent to McMaster Analytical X-Ray Diffraction Facility (MAX) for XRD analysis using a Bruker D8 DISCOVER cobalt source tube (Co-XRD) with a DAVINCI.DESIGN diffractometer. The diffractometer was set at 35 kV and 45 mA, with a 1 mm slit and 1 mm collimator, with data collected on a VANTEC-500 area detector with a 20 cm working distance. Each sample scan included 4 frames (900 seconds per frame) at 3 separate sample areas over a 2θ range of 10-88°. The 2D frames were collected with DIFFRAC.MEASUREMENT Centre Version 6.5 software, and patterns were integrated to 1D using DIFFRAC.EVA Version 4.2.

Transmission Electron Microscopy (TEM)

Freshly subsampled precipitates were diluted in anoxic water with a $\text{pH} \pm 0.1$ of the measured condition before pipetting 15 μL of diluted slurry onto lacey carbon coated 300-mesh Cu TEM grids. We allowed residual solution to evaporate prior to analysis, drying in the glovebox under anoxic conditions (< 0.1 ppm O_2), before storing the grids in TEM grid holders and anoxically heat sealing them in a mylar bag. The mylar bags were removed from the glovebox and shipped to Colorado School of Mines, Golden, Colorado, USA for analysis. Samples were examined on a Talos F200X at 200 keV for high-resolution imaging (HR-TEM) up to 0.12 nm, scanning transmission electron microscopy (STEM) imaging up to 0.16 nm, and Super-X window-less electron dispersive X-ray spectroscopy (EDS) analysis. Samples were imaged in high-angle annular dark-field (HAADF) to discern different phases. HR-TEM imaging was used to capture the crystal lattice spacing where the images were analyzed by Fast-Fourier Transformation (FFT) and Inverse FFT (IFFT) using Gatan DigitalMicrograph software. Additional structural data of individual phases was recorded by selected area electron diffraction (SAED). Elemental data was captured by the Talos F200X Super-X EDS detector for a minimum of ten minutes at each location. Bruker ESPRIT software Version 1.9 was used to analyze and quantify the EDS data by the Cliff-Lorimer method with a 1x2 binning where elemental quantification was ± 1 -10% of the presented values. Image contrast and brightness were adjusted to optimize image clarity. The raw EDS data for each experiment was recorded in Supplemental Table 1 and summarized in Table 6. In addition to our experimental samples, we analyzed a sample of cronstedtite, which was collected in Kisbanya, Hungary and provided from the Caltech Mineralogical Collection by G. Rossman, to determine how its measured elemental chemistry on the Talos F200X compared to the ideal formula for cronstedtite.

Results

Solution and Precipitate Chemical Analysis

Over the course of this experimental set-up, we measured the pH and extent of iron oxidation in the control and bubbled experiments. The ferrous control experiment after 19 days at 25 °C had a measured pH of 7.14 (Table 3). This experiment had no observable precipitate but after fully acidifying the experimental solution to dissolve any minor solids or colloids, we determined it contained 0.07 Fe(III)/FeT in bulk (Table 4). After a total of 40 days, the 25 °C control had a measured pH of 7.17 (Fig. 2; Table 3). The room temperature control had no visible color change and yielded no precipitate from which to obtain a Fe(III)/FeT precipitate measurement.

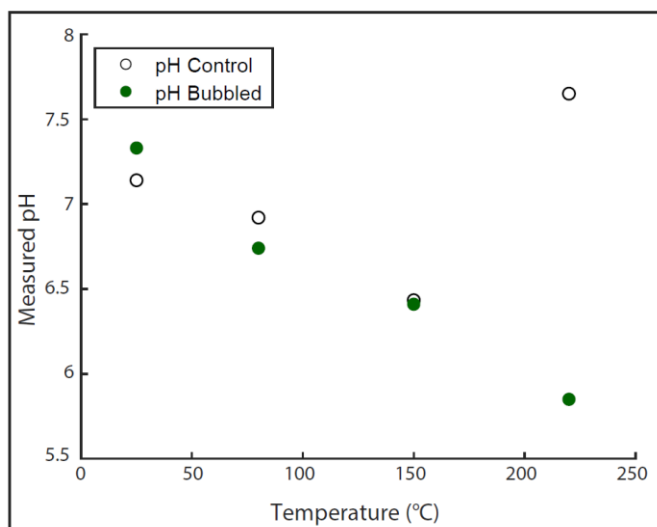


Figure 2. Plot of pH measurements from Parr vessel with precipitate and overlaying solution for control and bubbled experiments for temperatures that ranged from 25 - 220 °C. Note the uncertainty of the pH measurements and oven temperatures was ± 0.02 pH units and ± 0.4 °C respectively.

Increased hydrothermal temperatures can mimic diagenesis by either inducing higher-temperature reactions such as those that take place during sediment burial and/or simulating the effects of lower diagenetic temperatures over longer geologic time periods (Siever 1986). The control experiment that aged for an additional 7 days at 80 °C had a measured pH of 6.92 (Fig. 2; Table 3). The 80 °C control continued to not display any color change in solution and did not produce a precipitate for Fe(III)/FeT measurement. The control experiment subject to an additional 7 days at 150 °C had a pH of 6.43 (Fig. 2; Table 3). This 150 °C control did produce a minuscule amount of dark tan-green material that had 0.27 Fe(III)/FeT (Fig. 3; Table 5). The control experiment aged for an additional 7 days at 220 °C was measured to have a pH of 7.65 (Fig. 2; Table 3). This 220 °C control experiment precipitated a small amount of dark tan-green solid material with 0.32 Fe(III)/FeT (Fig. 3; Table 5).

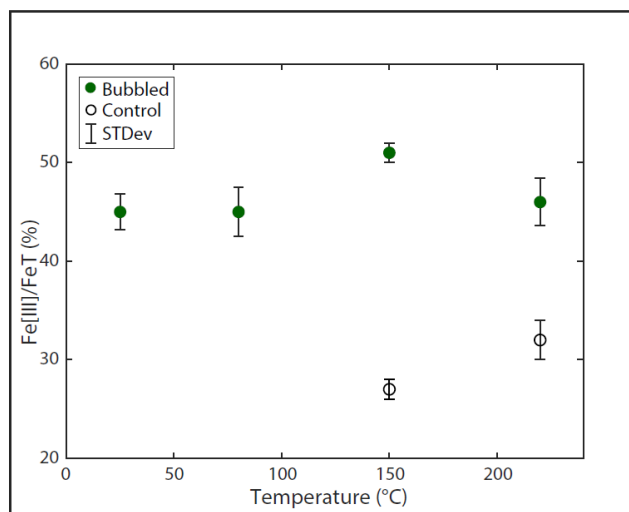


Figure 3. The measured Fe(III)/FeT content of the acidified control precipitates and bubbled precipitates along with the calculated standard deviation from replicate measurements.

We induced partial in situ iron(II) oxidation by bubbling trace levels of O₂ gas into Archean ocean solutions for a limited amount of time, and then simulated progressive diagenesis of the partially oxidized precipitates. After 19 days at 25 °C, the acidified and fully dissolved replicate bubbled experiment contained 0.75 Fe(III)/FeT in bulk (dissolved precipitate plus solution) (Table 4). This bubbled experimental solution had a pH of 7.33 and it had produced a green precipitate, suggesting a Fe(II-III) phase or phases (Velde 2003) (Table 3). Indeed, our ferrozine assay determined that this green precipitate contained 0.48 Fe(III)/FeT (Table 4). After an additional 21 days, and 40 days total, the bubbled experiment aged at 25 °C had a solution pH of 7.06 (Fig. 2; Table 3) and still contained a green precipitate. When we harvested and fully acidified a portion of this low-temperature bubbled precipitate, it contained 0.45 Fe(III)/FeT (Fig. 3; Table 5).

The bubbled experiment subject to aging at 80 °C for 7 additional days had a pH of 6.74 (Fig. 2; Table 3) and continued to yield a green precipitate. This 80 °C solid was measured to also have 0.45 Fe(III)/FeT (Fig. 3; Table 5). The bubbled experiment that was further aged at 150 °C had a measured pH of 6.41 (Fig. 2; Table 3). This 150 °C experiment continued to display a green precipitate and the acidified solid subsample had 0.51 Fe(III)/FeT (Fig. 3; Table 5). The bubbled experiment that was aged at 220 °C for an additional 7 days had a measured pH of 5.85 (Fig. 2; Table 3). This bubbled 220 °C experiment produced a slightly darker green-black precipitate with 0.46 Fe(III)/FeT (Fig 3; Table 5).

Bulk Mineralogy: XRD and Magnetic Response

Control experiments at 150 °C and 220 °C did not produce enough precipitate for analysis by XRD. XRD measurements of bubbled precipitates aged for 40 days at 25 °C produced a broad diffraction peak corresponding to the Kapton tube it was measured in but no other diffraction peaks, suggesting an amorphous to minimally crystalline product (Fig. 4). After 80 °C aging, the bubbled experiment contained three weak diffraction peaks consistent with a serpentine group silicate such as greenalite or cronstedtite and a spinel group oxide like magnetite (Fig. 4). After the 150 °C treatment, bubbled experiments displayed a heightening of the peaks observed at 80 °C along with the formation of additional peaks corresponding to a serpentine group silicate and spinel group oxide (Fig. 4). The bubbled experiment subject to 220 °C aging showed a continued narrowing of the diffraction peaks for a serpentine group silicate and spinel group oxide, reflecting an increase in crystal size and/or crystallinity (Fig. 4).

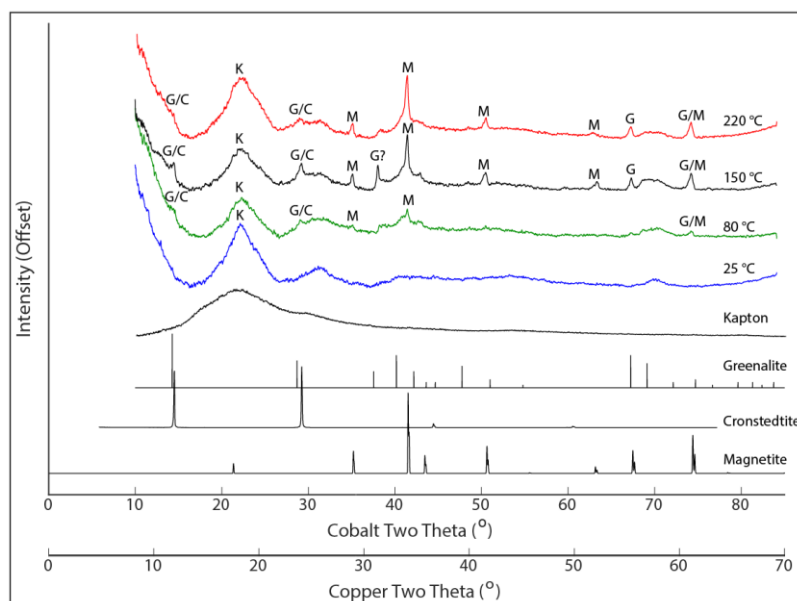


Figure 4: Cobalt sourced XRD patterns from replicate bubbled experimental precipitates subject to simulated diagenesis at 25 °C (Blue), 80 °C (Green), 150 °C (Black), and 220 °C (Red). Plotted for comparison: blank kapton tube (K); 1:1 iron-silicates greenalite (G), $[\text{Fe}^{2+}_3\text{Si}_2\text{O}_5(\text{OH})_4]$ (from Guggenheim et al. 1982) and cronstedtite (C), $[(\text{Fe}^{2+},\text{Fe}^{3+})_3(\text{Si},\text{Fe}^{3+})_2\text{O}_5(\text{OH})_4]$ (Lab Standard, Caltech Mineralogical Collection); and a spinel group iron-oxide, magnetite (M), $[\text{Fe}^{2+}\text{Fe}^{3+}_2\text{O}_4]$ (from Haavik et al. 2000). Both the copper and cobalt two theta axes are plotted for comparison. The experimental and standard diffraction patterns were vertically offset for clarity.

Control and bubbled experimental precipitates across the range of temperature displayed different degrees of magnetic attraction. The control 150 °C and 220 °C dark tan-green precipitates were both weakly to moderately attracted to the magnet (Fig. 5a & 5b). The bubbled green precipitate at 25 °C after a total of 40 days was not attracted to the magnet (Fig. 5c). However, after 7 days at 80 °C, the green precipitate was weakly attracted to the magnet (Fig. 5d). After an additional 7 days at 150 °C, the bubbled green precipitate was strongly attracted to the magnet (Fig. 5e). Seven days of aging at 220 °C produced the darkest green precipitate, which was the most attracted to a magnet compared to all our experimental samples (Fig. 5f).

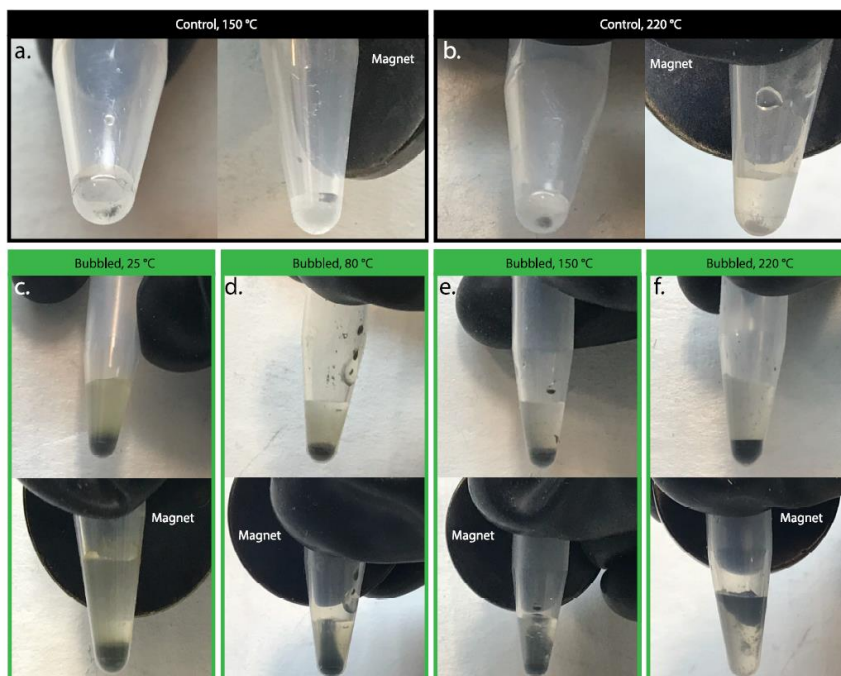


Figure 5: The precipitate from the 150 °C control experiment had a tan color (**a**-left) and was moderately attracted to the magnet (**a**-right). The precipitate from the 220 °C control experiment continued to have a tan color (**b**-left) but only some particles appeared to be attracted to the magnet (**b**-right). The precipitate from the bubbled experiment after aging at 25 °C had a green color (**c**-top) and was not attracted to the magnet (**c**-bottom). The bubbled experiment harvested after aging at 80 °C was green (**d**-top) and was moderately attracted to the magnet (**d**-bottom). The bubbled 150 °C precipitate was dark green (**e**-top) and continued to be moderately attracted to the magnet (**e**-bottom). The bubbled 220 °C precipitate was darker green (**f**-top) and was highly attracted to the magnet (**f**-bottom).

Electron Microscopy Characterization

Our TEM-EDS measurements of a cronstedtite standard (Supplemental Table 1) yielded high Fe+Mg, totaling ~30 at.% comparable to the ideal 29 at.% for cronstedtite and distinct from greenalite's 21 at.% Fe+Mg. However, the standard showed Si of ~9 at.%, slightly higher than the theoretical 7 at.% Si in cronstedtite from its formula but substantially lower than the calculated 14 at.% Si in greenalite. We also measured much lower O (54 at.%) in the cronstedtite standard compared to the expected 64 at.% O in both cronstedtite and greenalite. These results from the standard suggest that O is too light for accurate TEM-EDS measurements, but Fe, Mg, and Si measurements should be reasonable estimates of actual abundance in our samples. From their formulas, Mg-containing greenalite ($\text{Mg}^{2+}, \text{Fe}^{2+}$)₃Si₂O₅(OH)₄ should have a (Fe+Mg)/Si ratio of 1.5, while Mg-containing cronstedtite ($\text{Mg}, \text{Fe}^{2+}, \text{Fe}^{3+}$)₃(Si, Fe³⁺)₂O₅(OH)₄ should have a ratio of 4. The cronstedtite standard had an average (Fe+Mg)/Si of 3.3, somewhat lower than the ideal ratio of 4 set by the empirical formula of cronstedtite but reflecting the higher measured Si, and likely lower Fe³⁺, than in ideal cronstedtite.

Unlike the 25 °C–aged and 80 °C control experiments that did not produce a precipitate for analysis, after 7 days at 150 °C, the control contained a miniscule amount of tan precipitate (Fig. 6a). TEM imaging of the 150 °C control revealed abundant ~500 nm clusters composed of poorly formed tubular spindles with a width <10 nm and length <20 nm (Fig. 6b-6d). The tubular spindles were mainly composed of Mg (22 at.%), Si (21 at.%), O (38 at.%), moderate-low levels of adsorbed ions (3 at.% Na, 2 at.% K, 4 at.% Cl) and had an average $(\text{Fe}+\text{Mg})/\text{Si} = 1.6$ reflecting a Mg-phyllsilicate-like composition (Table 6). In one instance near the edge of the tubular spindle, we captured lattice spacing of 2.4 Å and 2.5 Å (Fig. 6d & 6d-i.), consistent with lattice spacings of a serpentine group mineral. Together with the lattice spacing, the tubular form was potentially consistent with a precursor version of fibrous chrysotile, a magnesium silicate in the serpentine group (Keeling et al., 2010).

In other regions of the 150 °C control, we observed poorly layered particles with 3-5 layers that were <5 nm wide and <50 nm long and highly susceptible to beam damage (Fig. 6e & 6f). We measured the lattice spacing for one of these structures to be 6.9 Å while another featured a 3.4 Å (003) plane adjacent to a 7.2 Å layered structure (Fig. 6f). Elemental analysis of these poorly layered structures showed 20 at.% Fe, 8 at.% Mg, and 8 at.% Si (Table 6). Additionally, we imaged a cluster of well-ordered blunt edged rods, <20 nm wide and 100-150 nm long, in this sample (Fig. 6h). These rods had a lattice spacing of 6.2 Å (Fig. 6k) and elemental analysis indicated that they were primarily composed of Fe (30 at.%) and O (46 at.%) (Fig. 6i-6j; Table 6), suggesting an iron oxide mineral. This iron oxide phase also exhibited a lath morphology ~20 nm wide and ~100 nm long (Fig. 6l) with a lattice spacing of 3.2 Å and 6.1 Å (Fig. 6l-i. and 6l-ii.). Neither the blunt edged rods or laths were degraded by the electron beam during analysis. SAED on a region containing these blunted rods and laths produced a polyanocrystalline pattern (Fig. 6m) consistent with the iron oxide lepidocrocite.

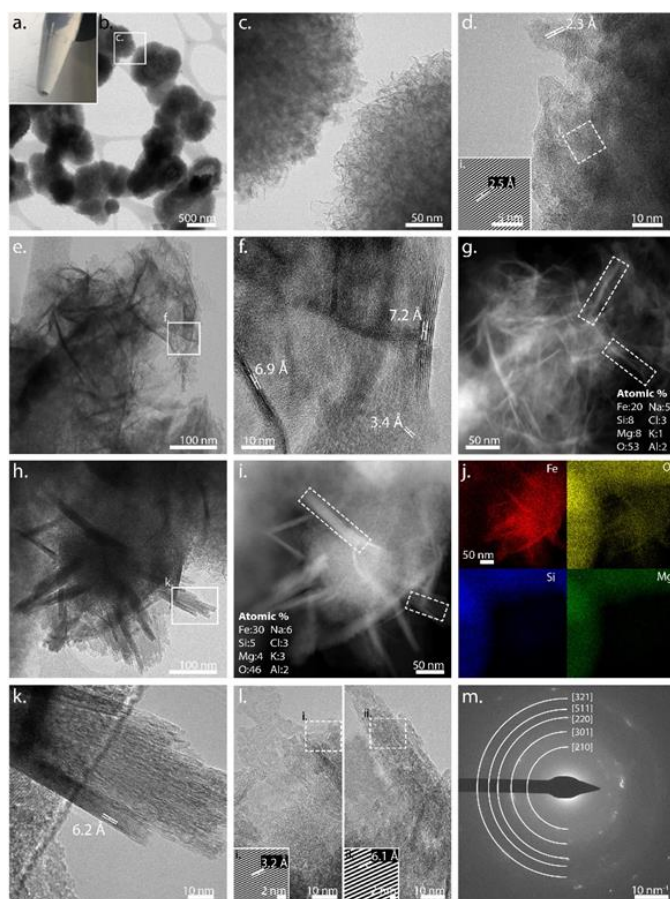


Figure 6: Tan precipitate harvested from control experiment after 7 days at 150 °C **(a)**. Clumps of heterogeneous particles included: poorly formed tubular spindles **(b-c)** with a 2.3 Å **(d)** and 2.5 Å **(d-i)** lattice spacing; layered structures with frayed edges **(e)** where the two particles had 6.9 Å and 7.2 Å lattice spacings **(f)** and measured elemental chemistry **(g)**; Table 6); blunt-edged rods **(h)** and the measured elemental chemistry **(i-j)**; Table 6). Basal spacing of the blunt-edge rods was measured to be 6.2 Å **(k)**, similar to another phase with a lathe-like morphology **(l)** and 3.2 Å and 6.1 Å lattice spacing **(l-i. & l-ii.)**. The polyanacrystalline SAED pattern from a region containing blunt-edged rods and lathes was most consistent with lepidocrocite **(m)**.

The control experiment further aged at 220 °C for 7 additional days also contained a small amount of tan precipitate (Fig. 7a). TEM images of the 220 °C control experiment showed abundant ~100-200 nm long hollow tubes with 0.6-0.8 nm inner diameters and 2-2.8 nm outer diameters (Fig. 7b-7d & 7f-7g). The elemental chemistry of these tubular structures was primarily Mg (21 at.%), O (65 at.%), and Si (8 at.%), suggesting a magnesium silicate (Fig. 7e; Table 6). Along the tube axis, we were able to capture two separate instances of 7.2 Å lattice spacing and higher order lattice planes of 3.6 Å (004) and 2.4 Å (006) (Fig. 7f & 7g-i.). Another tube at a different orientation captured the 4.3 Å (111) lattice plane of this phase (Fig. 7g-ii.). SAED of the control 220 °C experiment on a broad region composed mostly of tubes produced diffraction halos, suggesting a poorly crystalline phase (Fig. 7j). This tubular phase had an

elemental chemistry, lattice spacings, and SAED pattern consistent with a precursor magnesium serpentine, proto-chrysotile.

TEM analyses of the 220 °C control experiment also captured a ~100 nm wide globular phase (Fig. 7h). The elemental data of this phase indicated that it primarily contained Fe (24 at.%) and O (56 at.%) (Fig. 7h-7i; Table 6), suggesting an iron oxide. Additionally, the broad SAED of the 220 °C control experiment had distinct diffraction planes (manifesting as dots) that corresponded to the lattice spacings of 2.9 Å (220), 1.4 Å (440), and 1.0 Å (553) (Fig. 7j). These lattice planes captured by SAED in tandem with an elemental chemistry rich in iron and oxygen lead us to tentatively identify the globular phase as a spinel group iron oxide. With its globular morphology rather than the platelet morphology of the magnetite in the bubbled 220 °C experiment, it is possible that this phase was not magnetite but instead was a different spinel group oxide.

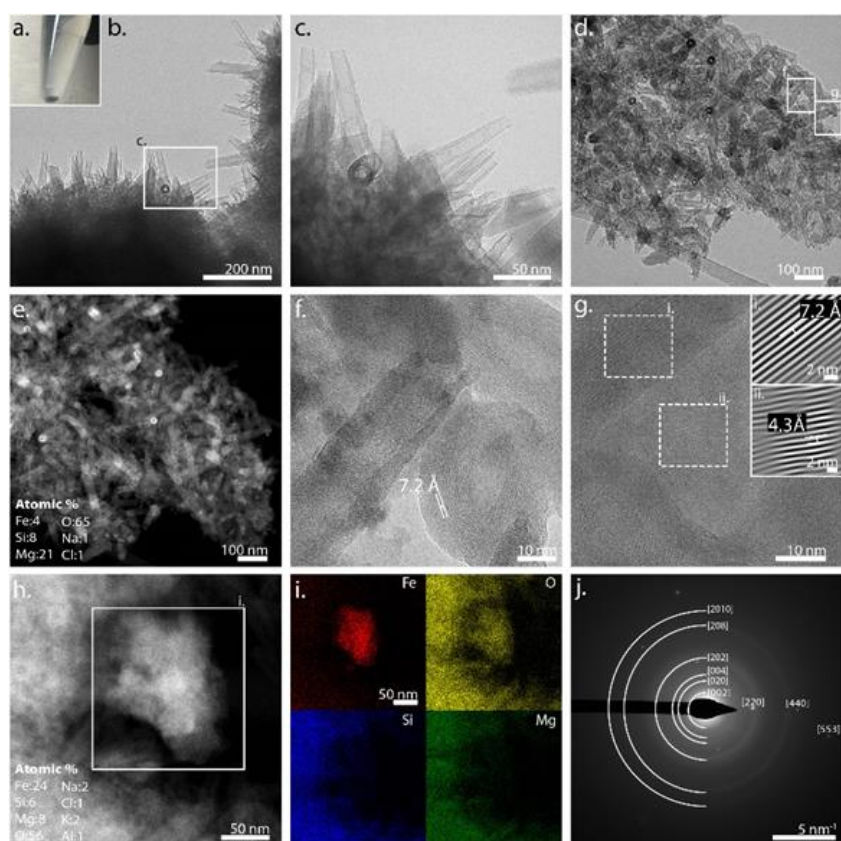


Figure 7: Tan precipitate harvested from control experiment after aging for 7 days at 220 °C (a). Homogenous clumps composed of hollow tubes (b-d) and measured elemental chemistry (e). Viewing down the tube axis and along the profile of the tube we measured the lattice spacing to be 7.2 Å in both instances (f & g-i.) and 4.3 Å at a separate orientation (g-ii.). A globular phase was observed (h) and elemental chemistry rich in Fe and O was mapped (i). SAED of a region containing both the tubular and globular phase respectively produced a polyanocrystalline pattern for a magnesium-silicate and planes for a spinel group, iron-oxide (j).

We additionally imaged the bubbled precipitates at temperatures 25-220 °C using TEM. Analysis of the 40-day-old 25 °C precipitate revealed a homogenous distribution of poorly layered spindly particles ~2-4 nm wide and ~20 nm long (Fig. 8b-8f). These structures were highly susceptible to beam damage, but we were able to capture four representative particles, each with a maximum of 3-4 layers that had an approximate lattice spacing of ~7.2-7.7 Å (Fig. 8d i.-ii. & 8f i.-ii.) measured by IFFT. SAED on a cluster of poorly layered particles produced a diffuse halo pattern corresponding to 1.3 Å, 1.5 Å, and 2.6 Å lattice spacings (Fig. 8g). The diffuse SAED halos in the bubbled 25 °C experiment reflect the formation of a poorly crystalline phase, consistent with the lack of peaks by XRD (Fig. 4). In addition, we measured the elemental chemistry of these poorly layered particles at three separate locations. EDS of the precipitates yielded a compositional range of 15-24 at.% Fe, 15-19 at.% Si, 1-3 at.% Mg, 46-58 at.% O, along with trace amounts of Na, Cl, K and Al (Fig. 8h-8j; Table 6). From this data, we calculated an average (Fe+Mg)/Si ratio of 1.2 for these poorly layered particles (Table 6). The observed morphological, structural, and elemental data suggested this phase was a Fe-rich proto serpentine.

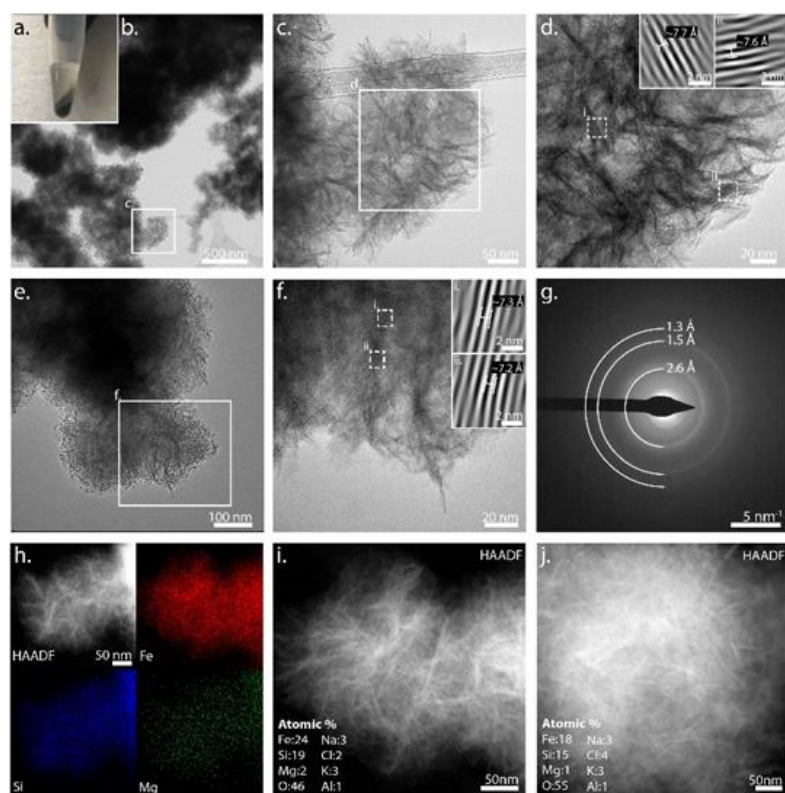


Figure 8: TEM-based observations of green precipitate (a) harvested from the bubbled experiment held at 25 °C for 40 days. Homogeneous distribution of particles with a spindly morphology (b-f) where the best captured particles exhibited a maximum of 3-4 layers (d & f) with an approximate basal spacing of ~7.2-7.7 Å determined by IFFT (d-i., d-ii., f-i., & f-ii.). SAED on a region of poorly layered particles produced diffuse rings corresponding to 1.3 Å, 1.5 Å, and 2.6 Å lattice spacings (g). HAADF image of poorly layered particles (h-j) with

corresponding EDS maps of Fe, Si, and Mg (**h**); the average atomic values are reported in Table 6.

Experimental Condition:	Fe	Si	O	Mg	K	Na	Cl	Al	Fe:Si	Fe:Mg	(Fe+Mg)/Si	Fe/(Fe+Mg)
Bubbled 25 °C Poorly Layered	18.97	16.90	52.77	1.90	3.14	2.72	2.59	0.91	1.12	9.96	1.24	0.91
Bubbled 80 °C Well Ordered Layered	25.34	11.81	57.45	1.47	0.94	0.85	1.21	0.93	2.15	17.27	2.27	0.95
Bubbled 150 °C Well Ordered Layered	22.16	15.05	53.60	4.54	1.38	1.06	1.43	0.77	1.47	4.88	1.77	0.83
Bubbled 220 °C Well Ordered Layered	16.63	15.75	48.05	10.23	2.52	3.67	2.23	0.92	1.06	1.63	1.71	0.62
Bubbled 220 °C Spinel Group Oxide	23.04	10.96	49.28	9.41	1.41	2.85	1.43	1.63	2.10	2.45	2.96	0.71
Control 150 °C Poorly Layered	10.67	20.61	37.73	21.52	1.78	2.81	4.24	N/A	0.52	0.50	1.56	0.33
Control 150 °C Lepidocrocite	30.21	4.8	46.19	4.4	3.09	5.82	3.17	2.27	6.29	6.87	7.21	0.87
Control 220 °C Chrysotile	3.88	7.68	64.70	20.64	0.13	1.84	0.49	0.64	0.50	0.19	3.19	0.16
Control 220 °C Spinel Group Oxide	23.23	6.95	55.72	8.59	1.37	1.77	1.15	1.24	3.34	2.70	4.58	0.73

Table 6. Summary of the average elemental composition of the phases (in atomic % or as a ratio) at each experimental condition.

TEM imaging of the bubbled experimental precipitate aged at 80 °C for 7 additional days revealed well-ordered bladed crystals ~100 nm wide and ~300-700 nm long (Fig. 9b-9d). We measured the lattice fringe of the bladed structures to be 7.2 Å (Fig. 9c & 9f). TEM also revealed multiple instances of a triangular-trapezoidal form (Fig. 9b, 9g, 9j) where the well-ordered regions had a 7.0 Å lattice fringe (Fig. 9j-i.). The bladed and triangular-trapezoidal structures together exhibited an average elemental chemistry (Fe+Mg)/Si of 2.3 with low Mg (1.5 at.%) consistent with an iron silicate within the cronstedtite-greenalite solid solution (Fig. 9d-9e, 9h-9i; Table 6). The large remaining portion of the structure exhibited multiple crystal defects restricting the number of ordered layers (Fig. 9k); however, we did measure a 7.2 Å lattice fringe (Fig. 9k-i.). SAED on an area containing the bladed and trapezoidal structures produced recurring diffraction planes congruous with a serpentine group silicate (Fig. 9l). TEM analysis also captured ~50-70 nm wide platelets with a characteristic 4.7 Å basal spacing (Fig. 9m) along with additional lattice planes by FFT (Fig. 9m-i.) corresponding to a spinel group phase such as magnetite.

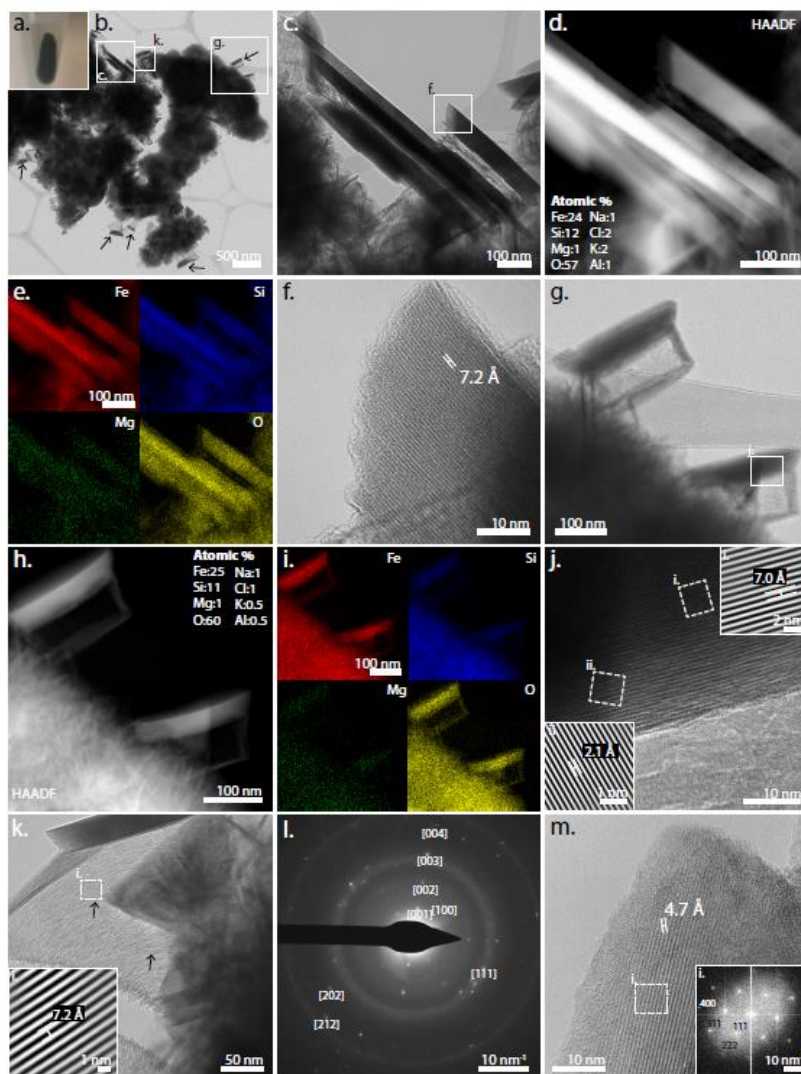


Figure 9: TEM analyses of green precipitate **(a)** harvested from bubbled experiment after 7 days at 80 °C. We observed a heterogeneous mixture of morphologies, including well-ordered blades **(b & c)** with the elemental chemistry maps shown for Fe, Si, Mg, and O **(d & e)**, also see Table 6), containing a 7.2 Å lattice fringe **(f)**; triangular-trapezoidal structures **(b-arrows, g, j, k)** showing Fe, Si, Mg, and O chemical maps **(h & i)**. In this phase, the “caps” of the structure **(j)** had 7.0 Å and 3.1 Å **(j-i. & j-ii.)** while the “body” of the structure **(k)** had frequent crystal defects **(k-arrows)** and 7.2 Å lattice spacing **(k-i.)**. SAED of a heterogeneous area similar to panel b produced recurring lattice planes **(l)**. A third morphology observed were platelets that had a 4.7 Å lattice fringe **(m)** and multiple FFT lattice spacings corresponding to a spinel group phase such as magnetite **(m-i.)**.

TEM analysis of the bubbled sample at 150 °C for an additional 7 days displayed well-ordered layered structures ~100-200 nm long and ~10-50 nm wide (Fig. 10b). We measured 7.1-7.3 Å basal spacing in three separate particles (Fig. 10d, 10d-i., 10f). In one instance, a well-ordered layered particle was in the proper orientation to capture both its basal lattice spacing of

7.1 Å (Fig. 10f) and 24 Å superlattice (Fig. 10f-i.). Using elemental data on three regions containing layered structures, we calculated an average (Fe+Mg)/Si = 1.8 with a Mg content of 4.5 at.% (Table 6). Collectively, the TEM data demonstrated that these structures were greenalite-like minerals. TEM imaging also showed a second phase of overlapping ~10-20 nm wide platelets with a basal lattice spacing of 4.7 Å (Fig. 10g). FFT on the area containing the platelets revealed lattice spacing planes of 4.8 Å (111), 2.4 Å (222), 1.6 Å (333), and 2.5 Å (311) (Fig. 10g-i.), consistent with a spinel group phase like magnetite.

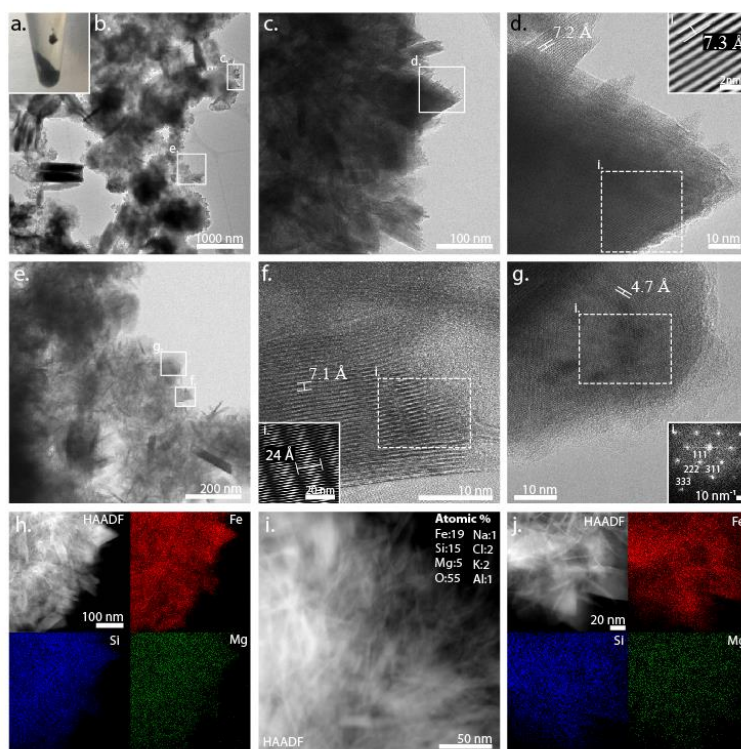


Figure 10: Observations of the dark green precipitate (a) harvested from a bubbled experiment after 7 days at 150 °C. TEM revealed a heterogeneous mixture of phases (b) containing well-ordered blades (c-f) where the lattice spacings were measured to be 7.2 Å (d) and 7.3 Å (d-i.). Some particles showed a basal lattice spacing (001) 7.1 Å (f) and 24 Å superlattice modulation (f-i.). We also observed a platelet phase with 4.7 Å lattice spacing (g) where FFT confirmed the presence of lattice planes consistent with a spinel group iron-oxide like magnetite (g-i.). The elemental chemistry of the layered blades indicated a phase rich in Fe and Si with a small amount of Mg (h-j; Table 6).

TEM of the bubbled experiment after 7 days at 220 °C revealed ~400 nm clusters of well-ordered layered structures ~20-60 nm wide and ~100 nm long (Fig. 11b, 11c, 11e, 11f). We measured a basal lattice spacing of 7.1 Å in two separate layered particles (Fig. 11c & 11f), with one of these particle orientations also capturing a ~21 Å superlattice (Fig. 11f-i.). We determined the elemental composition of these layered structures over two regions, where we observed that the particles remained Fe and Si rich but the average Mg content had increased to 10% (Table 6).

This data enabled us to calculate the average (Fe+Mg)/Si of 1.7 (Table 6). Collectively, the TEM data demonstrated that these structures were greenalite-like minerals. TEM imaging also revealed ~30-50 nm wide platelets (Fig. 11h). FFT analysis on an area containing the platelets produced lattice spacing planes: 4.8 Å (111), 2.4 Å (222), 1.6 Å (333), 2.5 Å (311), and 1.7 Å (422), again consistent with a spinel group mineral like magnetite (Fig. 11h-i.). We captured elemental data from one region containing the platelet phase and observed that it was mainly composed of Fe (28 at.%), O (56 at.%), and Si (11 at.%) (Fig. 11h; Table 6) along with moderate levels of adsorbed cations (6 at.% Na, 4 at.% Mg, and 3 at.% K) (Table 6). We attribute the higher-than-expected measurement of Si to be the result of adsorbed Si (Philippini et al. 2006). The lattice spacing of the platelet paired with the elemental chemistry rich in Fe and O, in addition to the strong magnetic reaction of this and other bubbled and hydrothermally-aged precipitates, was most consistent with identifying this platelet phase as magnetite (Fig. 4).

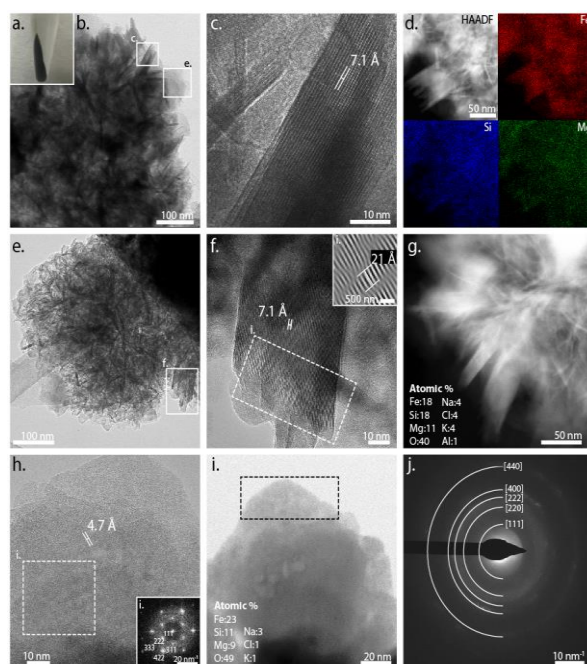


Figure 11: The bubbled experiment after 7 days at 220 °C yielded the darkest green precipitate (a). TEM revealed the heterogeneous phases (b) within this experiment that included well-ordered blades with a 7.1 Å lattice spacing (c) along with elemental chemistry rich in Fe, Si, and Mg (d). An additional example of this layered, bladed phase (e) showed a 7.1 Å d-spacing (001) with superlattice modulation of 21 Å (f & f-i.), and elemental chemistry (g). Additionally, we observed a platelet phase with 4.7 Å lattice spacing (h) and FFT lattice planes consistent with a spinel group identification (h-inset); we also show the measured elemental chemistry of the platelet (h-i.). SAED of an area containing the platelets displayed polyanocrystalline halos at the lattice planes of a spinel group mineral (j).

Synthesis of Experimental Results

Our ferrous control experiment set at pH 7 with 1:1 Fe:Si did not produce an observable precipitate from solution either at low temperature nor upon 80 °C hydrothermal aging. At 150 °C, we observed temperature-induced precipitation of abundant poorly ordered Mg-silicates (Fig. 6b-d, 6d-i.; Table 6), occasional lepidocrocite (Fig. 6h-6m), and a few examples of poorly formed ~ 7 Å iron-rich silicates (Fig. 6e-6g). Additional aging at 220 °C of the ferrous control mainly produced chrysotile nanotubes (Fig. 7b-7g, 7g-i., 7g-ii., 7j) and a spinel group iron-oxide (Fig. 7h-7j). During hydrothermal aging, the ferrous solution decreased in pH as temperature increased and minerals precipitated. The 25 °C solution had a pH of 7.17, which decreased to pH 6.74 at 80 °C, further decreasing to pH 6.43 at 150 °C (Fig. 2; Table 3). This decrease in pH can be attributed to the formation of an Fe(III) (hydr)oxide, such as the lepidocrocite that we observed (Fig. 6h-6m). Additionally, the precipitation of iron/magnesium silicate phases will take up hydroxide ions and release protons, also dropping the pH (Fig. 6e-6g; Zolotov 2014).

Low O₂ bubbled experiments examined in situ Fe(II) oxidation at pH 7 in the presence of silica produced a partially oxidized ($\sim 45\%$ Fe(III)/FeT) precipitate (Fig. 3). After 40 days at 25 °C, we characterized this homogenous phase as Fe-rich proto serpentine (Fig. 8b-8f). Aging of

the Fe-rich silicate phase at 80 °C produced a well-layered iron silicate (Fig. 9c-9f) and magnetite (Fig. 9g). Continued hydrothermal aging at 150 °C and 220 °C crystallized well-ordered greenalite with incorporated Mg (Figs. 10c-i.; 11b, 11c, 11e, 11f-i.; Table 6) and magnetite (Fig. 10g, 10h-i). With increasing temperature, the experimental solution pH decreased from a pH of 7.33 at 25 °C down to pH 5.85 at 220 °C (Fig. 2; Table 3). The continued decrease in pH can be attributed to the formation and crystallization of a well-ordered iron silicate (Figs. 4; 9c-9f; 10c-10f; 11b-11g) and the iron oxide magnetite (Figs. 4; 9m; 10g; 11h), similar to the control experiments.

Discussion

Impacts of Temperature on Ferrous Controls at Circumneutral pH

Our ferrous experiments under simulated silica-rich Archean ocean conditions at pH 7 did not produce a precipitate at low temperature. Other studies with Archean-relevant Fe(II) and Si concentrations produced iron(II) silicates at 25 °C, but only when the pH was elevated to ≥ 7.5 (Tosca et al. 2016; Farmer et al. 1991; Hinz et al. 2021). During the Fe(II) hydrolysis process, silica inhibits Fe(II) polymerization, resulting in smaller clusters of octahedral Fe(II) and a kinetic barrier to precipitation (Doelsch et al. 2002; Francisco 2020). Our observations of a lack of precipitation at ≤ 80 °C supports that a higher pH is required to induce iron(II) silicate formation under ferrous conditions at low temperature.

However, our ferrous experiment at 25 °C did contain a trace amount of Fe(III) (bulk Fe(III)/FeT = 0.07, Table 4), which would be expected to precipitate at circumneutral pH. The presence of any Fe(III) suggests there may have been slight O₂ contamination or a trace Fe(III) impurity in all of our experiments. Even with this minor amount of Fe(III), the lack of precipitate in this experiment is surprising since Fe(III) is highly insoluble at circumneutral pH and readily precipitates as ferric oxides or Fe(II,III) phases from solution. Under these Fe, Si, and pH conditions, we suspect that Fe(III) aquo complexes, such as Fe(III)-Si, Fe(OH)₂⁺, Fe(OH)CO₃, and FeCl²⁺ (Steffansson 2007; Perrson 2018), hosted the measured Fe(III). Kinsela et al. (2016) has shown the presence of silica—even an order of magnitude below the 1.1 mM Si used in this study—hinders Fe(II) oxidation at circumneutral pH. Therefore, the absence of precipitate at low temperature and 80 °C in our ferrous control experiments was likely the result of the presence of high dissolved silica and insufficient Fe(III) to trigger precipitation of ferric oxides or Fe(II,III) silicates as observed by Hinz et al. 2021.

Increased temperatures can influence chemical processes and induce mineral precipitation, and our results showed precipitation in the control precipitates at 150 °C that preferentially incorporated the trace dissolved Fe(III). At this elevated temperature, the control precipitate contained 0.27 Fe(III)/FeT (Fig. 3; Table 5). Indeed, we observed an iron oxide, lepidocrocite, formed at 150 °C under almost entirely ferrous conditions (Fig. 6h-6m). Soluble Fe(II) in the presence of poorly crystalline Fe(III) oxides like ferrihydrite is capable of catalyzing the reductive dissolution and secondary mineralization of more crystalline ferric oxides such as lepidocrocite or goethite (Burton et al. 2007; Cornell and Schwertmann 2003; Nitschmann 1938; Pedersen et al. 2005; Hansel et al. 2005). Therefore, we hypothesize that the higher 150 °C

temperature promoted the precipitation of ferric oxides from trace dissolved Fe(III), and, in the presence of abundant Fe(II), these initial oxides recrystallized into the lepidocrocite that we observed.

Our ferrous experimental observations at 150 °C also revealed the precipitation of a magnesium-rich silicate phase (Fig. 6b & 6c) and a minor amount of magnesium-rich iron silicates (Fig. 6e & 6f). While poorly ordered, the magnesium silicate (Table 6) with ~11 at.% iron was notably the most abundant phase and manifested in distinctive tube-like structures (Fig. 6c & 6d). Our ferrous 150 °C experiment also produced a poorly formed serpentine group iron silicate with 6.9-7.2 Å lattice spacing (Fig. 6e & 6f). Although we did not observe an iron-rich silicate in control experiments at any other temperature to provide a direct comparison, the results showed a notable amount of Mg inclusion (8 at.% Mg) in the iron silicate (Table 6). The extent of Mg incorporation into the silicate was comparable to iron silicates formed under ferrous conditions at pH 7.5 and aged to 150 °C, which contained 10.9 at.% Mg (Hinz et al. 2021).

After 220 °C aging, our ferrous control experiment was predominantly composed of chrysotile nanotubes (Fig. 7b-7g) and a globular iron oxide (Fig. 7h-7i). The widespread chrysotile at 220 °C suggests the transformation of the poorly formed 150 °C Mg-silicate to a more crystalline form. The elemental analysis of the chrysotile nanotubes showed they included 4 at.% Fe (Fig. 7e; Table 6). Chrysotile has been reported to host 2-3 weight % (wt.%) Fe (Bowes and Farrow 1997), where Fe(II) or Fe(III) are capable of being substituted into the octahedral site but only Fe(III) can be incorporated into the tetrahedral site (Walter et al. 2019). The incorporation of Fe into the chrysotile structure could have been aided by dissolution-reprecipitation reactions during the crystallization of Mg silicates into chrysotile. These reactions mineralizing chrysotile and releasing OH groups likely also buffered the solution to the higher pH of 7.65 that we measured in this experiment (Table 3; Fig. 2; Trittschack et al. 2014). There may have been substantial incorporation of Fe(III) into the chrysotile structure upon 220 °C aging, similar to what occurs during serpentinization (Evans 2008; Tutulo et al. 2021). Indeed, the Fe(III) content of the bulk precipitate increased from 27% at 150 °C to 32% at 220 °C. Alternatively, it is possible that most of the iron in chrysotile was Fe(II), and the majority of the measured 32% Fe(III) in solids was associated with the spinel group iron oxide (Fig. 7h-7i; Table 5). In the ferrous 150 °C experiment, we observed many small particles of the ferric oxide lepidocrocite, which could have reacted with Fe(II) during 220 °C aging to transform lepidocrocite into a spinel group iron-oxide phase (e.g., Postma 1993; Hansel et al. 2005).

In Situ Fe(II) Oxidation at Circumneutral pH

Broadly, our trace O₂ bubbling experiments highlight that in situ Fe(II) oxidation in the presence of silica produces an Fe-rich proto serpentine at pH 7 and 25 °C. The presence of a small proportion of Fe(III) under silica-rich conditions has been shown to induce precipitation, including of silicate phases (Hinz et al. 2021). This low-Fe(III) trigger provides an alternative mechanism for the formation of proto Fe-rich serpentine at low temperatures and the predicted lower pH of the Archean ocean. However, in our previous study, adding Fe(III) (aq) in the presence of silica at pH 7 and 25 °C produced mainly an amorphous phase with rare proto-silicates, with a bulk iron redox state of 0.89 Fe(III)/FeT (Hinz et al. 2021). Yet here, in situ Fe(II) oxidation at pH 7 induced the formation of a more ferrous (48% Fe(III)) and more homogeneous Fe-rich proto silicate at 25 °C (Fig. 8b-8f; Table 5).

Similar to the control experiments, our results from bubbled experiments suggested that there was additional Fe(III) dissolved in the solution. The acidified 25 °C bubbled solution-precipitate combination contained much higher Fe(III), measuring 0.75 Fe(III)/FeT, compared to the 0.48 Fe(III)/FeT in solids (Table 4). This higher bulk measurement possibly reflects that a portion of the Fe(III) was in Fe(III) aquo complexes, such as Fe(III)-Si, Fe(OH)₂⁺, Fe(OH)CO₃, and FeCl²⁺, similar to what we suspect occurred with the minor amount of Fe(III) in the control experiment solutions (Steffansoon 2007; Perrson 2018). The additional Fe(III) measured in solution could also be attributed to colloidal Fe(II,III) phases such as silicates, green rusts, or Fe(III) oxides. The Fe(III) discrepancy between the precipitate compared to bulk redox state implies that we cannot discount the impact that these dissolved or colloidal Fe(III) sources may have on mineral formation. However, the precipitates from bubbled experiments all exhibited a consistent extent of Fe(III) oxidation of 0.45-0.51 Fe(III)/FeT, regardless of aging conditions or temperatures (Fig. 3; Table 5). This Fe(III) stability in bubbled experiments across all temperatures suggests that there was not substantial incorporation of Fe(III) (aq) into the solid with increasing temperature.

Effects of Simulated Diagenesis on Fe(II,III) Silicates

Upon hydrothermal aging, the initial 25 °C formation of iron proto silicates via in situ Fe(II) oxidation crystallized into a well-ordered iron serpentine phase accompanied by magnetite (Fig. 9c, 9f, 9j, 9m). To identify and understand the extent of crystallization of iron silicates, we must examine their structural characteristics. The structural measurements, including the 7 Å basal spacing, of the silicate products in bubbled experiments indicated they were serpentine group silicates, which are composed of alternating silica tetrahedral layers and metal-bound octahedral layers. The chemistry we observed in bubbled silicate products at all temperatures indicated that the principal metal ion was Fe, pointing to a serpentine group iron silicate, either Fe(II) greenalite or Fe(II,III) cronstedtite. One way to differentiate cronstedtite from greenalite stems from the fact that the Fe(II) in greenalite has a misfit between the tetrahedral and octahedral layers, resulting in a modulated structure (Guggenheim et al. 1982; Guggenheim and Eggleton 1998). This superlattice structure of greenalite has a ~23 Å modulation (Guggenheim et al. 1982; Guggenheim and Bailey 1989; Guggenheim and Eggleton 1998; Rasmussen et al. 2021; Johnson et al. 2018), in contrast to the ~17 Å superlattice periodicity of the Mn(II) serpentine endmember and the 33-38 Å modulation of the Mg serpentine antigorite (Guggenheim et al. 1982; Capitani and Mellini 2004). Conversely, the Fe(III) within the cronstedtite structure has a smaller ionic radius than Fe(II) or Mg. The Fe(III) substitution for silica at the tetrahedral site stabilizes the layered configuration and restricts structural modulation; therefore, the ~23 Å superlattice is not observed in cronstedtite (Caruso and Chernosky 1979; Wicks and O'Hanley 2018; Hybler, 2000). Additionally, the Fe(III) substitution at the silica tetrahedra site in cronstedtite increases its ideal (Fe+Mg)/Si ratio to 4 compared to 1.5 for greenalite, providing an additional way to identify the iron serpentine mineralogy.

We can thus further infer the placement of the experimental silicates at various temperatures along the greenalite-cronstedtite solid solution, as well as their Fe(III) content, by their measured (Fe+Mg)/Si ratio. To characterize the composition of the silicates and where they fall along the cronstedtite-greenalite solid solution, we used the defined formulas for both endmembers, Mg-containing greenalite [(Fe²⁺,Mg)₃Si₂O₅(OH)₄] and Mg-containing cronstedtite [(Fe²⁺,Fe³⁺,Mg)₃(Si,Fe³⁺)₂O₅(OH)₄], and compared the (Fe+Mg)/Si ratio of our cronstedtite

standard and samples against the idealized ratios from mineral formulas. Mg-containing greenalite $(\text{Fe}^{2+}, \text{Mg})_3\text{Si}_2\text{O}_5(\text{OH})_4$ would have a $(\text{Fe}+\text{Mg})/\text{Si}$ ratio of 1.5, while Mg-containing cronstedtite $(\text{Fe}^{2+}, \text{Fe}^{3+}, \text{Mg})_3(\text{Si}, \text{Fe}^{3+})_2\text{O}_5(\text{OH})_4$ would have a ratio of 4. The cronstedtite standard had an average $(\text{Fe}+\text{Mg})/\text{Si}$ of 3.3, somewhat lower than the ideal ratio of 4 set by the empirical formula, reflecting the higher measured Si than in ideal cronstedtite. The proto silicate precipitated at 25 °C had an $(\text{Fe}+\text{Mg})/\text{Si}$ of 1.2, below the theoretical $(\text{Fe}+\text{Mg})/\text{Si}$ ratio for greenalite of 1.5 due to its elevated Si content (Fig. 12a; Table 6). This higher Si content in the initial, poorly-ordered form of the proto iron silicate was similarly observed in prior studies (Tosca et al. 2016; Hinz et al. 2021).

At 80 °C, we observed the crystallization of a 7 Å iron silicate (Fig. 9c, 9f, 9j; Table 6) with much lower relative Si, averaging an $(\text{Fe}+\text{Mg})/\text{Si}$ of 2.3, which falls between cronstedtite and greenalite. Additionally, the 80 °C cronstedtite-greenalite displayed a pseudo-triangular morphology and lacked any indication of a superlattice despite being well-crystallized (Fig. 9b-arrows & 9k), consistent with observations from similar cronstedtite formation studies (Pignatelli et al. 2013 and Vachner et al. 2019). Based on the defined endmember formulas, the bubbled 80 °C layered precipitate with $(\text{Fe}+\text{Mg})/\text{Si}$ of 2.3 was characterized as a 30% cronstedtite and 70% greenalite solid solution (Table 6). Assuming all the measured Fe+Mg was Fe^{2+} or Fe^{3+} , which is not too inaccurate considering this sample only contained 1.5 at.% Mg on average, and assuming that this Fe was equally split between the two redox states, our calculated proportion of cronstedtite would suggest that this 80 °C-crystallized phyllosilicate contained approximately 15% Fe(III).

Therefore, there appears to be a transition from a high-Si Fe(II,III) silicate at low temperatures to a crystalline phase within the solid solution between Fe(II) greenalite and Fe(II,III) cronstedtite at 80 °C. Intriguingly, the $\Delta G_{\text{formation}}^\circ$ for cronstedtite has been found to be favorable at temperatures < 120 °C, high Fe/Si ratios, and circumneutral pH, similar to our experimental conditions (Zolotov 2014; Pignatelli et al. 2013, 2014; Vachner et al. 2019). However, additional recrystallization and mineralization at higher temperatures appeared to alter the silicate phase further.

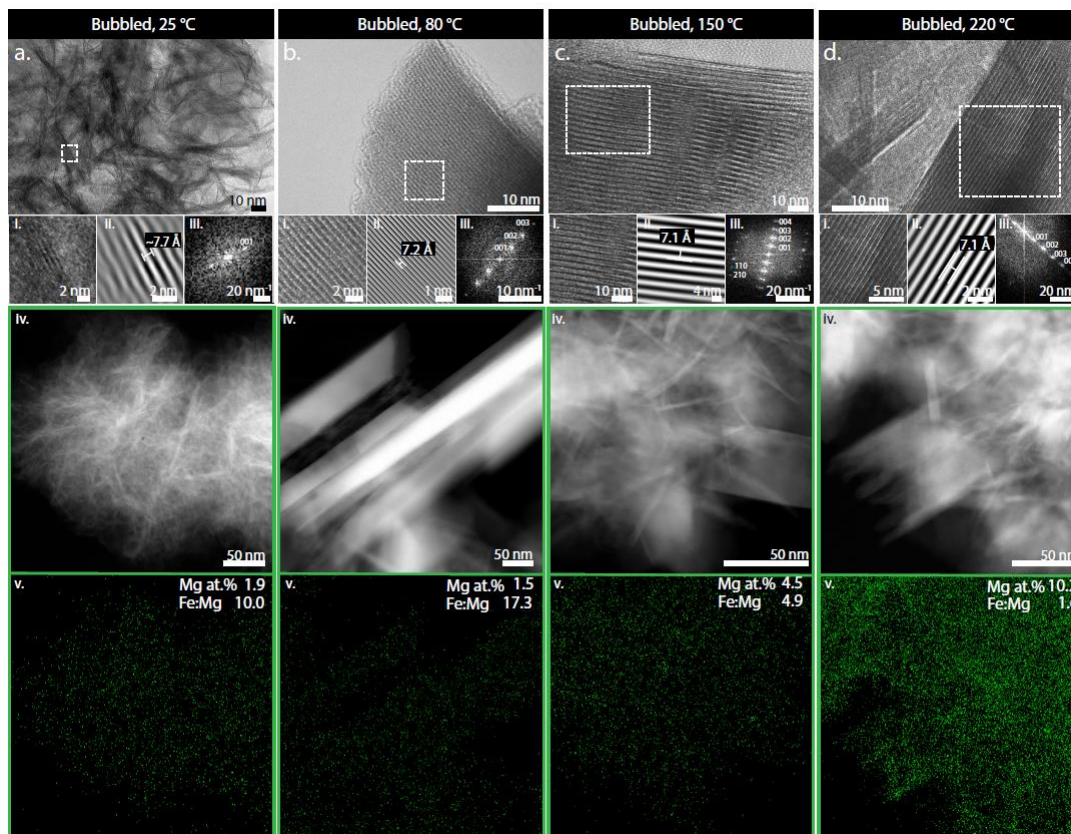


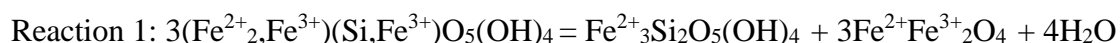
Figure 12: Compilation of the layered phase observed in bubbled experiments at temperatures 25, 80, 150 and 220 °C. At 25 °C, we observed spindly particles (**a**) with a maximum of 4 layers (**a-i**) measured with an approximate lattice spacing of 7.7 Å by IFFT (**a-ii**) with FFT only showing the basal d-spacing (001) (**a-iii**). Cluster of poorly layered particles in HAADF (**a-iv**) and Mg distribution and content on average (**a-v**). At 80 °C, we observed well-ordered particles (**b**) with extensive layering (**b-i**) with a lattice fringe of 7.2 Å as measured by IFFT (**b-ii**) and showing multiple lattice planes by FFT (**b-iii**). Region with well ordered layered blades in HAADF (**b-iv**) and Mg distribution and average content (**b-v**). We observed similar well-ordered particles at 150 °C (**c**) with extensive layering (**c-i**) where the lattice fringe was 7.1 Å by IFFT (**c-ii**) and displayed recurring lattice planes by FFT (**c-iii**). Collection of well-ordered particles in HAADF (**c-iv**) alongside Mg distribution and content (**b-v**). At 220 °C, we continued to observe a well-ordered layered phase (**d & d-i**) with a measured lattice fringe of 7.1 Å by IFFT (**d-ii**) and recurring lattice planes by FFT (**d-iii**). Collection of well-ordered particles in HAADF (**d-iv**) and Mg distribution and content (**d-v**).

In contrast to lower-temperature silicates, higher temperature (150-220 °C) aging produced an iron silicate characteristic of the greenalite endmember. In the abundant layered forms, we continued to observe 7 Å spacing typical of a serpentine group silicate (Figs. 10d, 10d-i., 10f; 11c, 11f). Additionally, the layered phase at both temperatures exhibited a 21-24 Å superlattice (Figs. 10f-i. & 11f-i.) and (Fe+Mg)/Si of 1.7-1.8 (Table 6) similar to ideal greenalite and not congruent with cronstedtite. Our results thus demonstrate that cronstedtite was not present in experiments ≥ 150 °C, supporting the hypothesis that cronstedtite does not form at higher temperatures (Vachner et al. 2019). Instead, we suggest the more Fe(III)-rich cronstedtite-

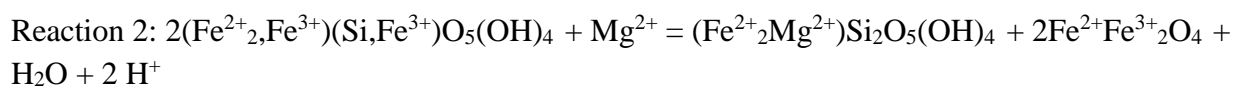
greenalite that initially crystallized at 80 °C reprecipitated into a more endmember Fe(II) greenalite at ≥ 150 C°.

Not only did the higher-temperature aging result in greenalite mineralization, but we observed a rising incorporation of Mg in the layered silicate. While the silicate had minimal magnesium at 25-80 °C (~1.5 at.% Mg), Mg increased to 4.5 at.% at 150 °C and 10 at.% at 220 °C (Fig. 12; Table 6). As there was only trace Mg in the lower temperature precipitates, this incorporated magnesium almost certainly originated from the solution, which contained 10 mM Mg to be analogous to Archean seawater. This Mg was likely dissolved until sufficiently high temperatures because of the very stable Mg hydration complex (Hostetler and Christ 1968; Sayles and Fyfe 1973). Similar to magnesium substitution into carbonate minerals during diagenesis, the Mg then partitioned into the iron silicate as its kinetic barriers to mineralization were overcome by increased temperature. Intriguingly, our observation of increasing Mg with continued aqueous alteration also follows the pattern of Mg enrichment during the aqueous alteration inferred in carbonaceous CM chondrites (Suttle et al. 2021; McSween 1979; Tomeoka et al. 1989; Howard 2011) and increasing Mg in serpentines during serpentinization alteration reactions (e.g., Evans 2008; Beard et al. 2009). Our experimental results therefore support the hypothesis that Mg will exchange for Fe²⁺ with progressive alteration, following the model of McSween (1979) and Tomeoka et al. (1989).

High temperatures (≥ 80 C°) not only impacted the specific silicate crystallized and extent of Mg incorporation, but this simulated diagenesis also promoted the formation of an iron oxide, magnetite. The increase in magnetite crystallization with higher temperatures was denoted by sharpened peaks in the XRD patterns (Fig. 4), TEM observations (Figs. 9m; 10g; 11h), and strengthening magnetic attraction (Fig. 5d-5f). Notably, the formation and proliferation of magnetite coincided with the increase in Mg incorporation into the silicate structure. This formation of a Mg-rich serpentine with related secondary magnetite mineralization is similar to reactions that occur in serpentinization, potentially due to the oxidation of Fe(II) serpentine or Fe(II)-bearing hydroxides by water (e.g., Evans 2008; Beard et al, 2009). However, in our experiments, our collective data suggest that it was Fe(II,III) phyllosilicates that relinquish ferric iron to form magnetite, following a reaction described by Zolotov (2014):



We argue that the increased crystallization of magnetite at high temperature is linked to the compositional and structural transformation of the silicate phase, including the incorporation of Mg. Our experiments were conducted in Parr vessels that represent a closed system; therefore, the total Si, Fe, and Mg should remain constant at each condition. As our 80 C° silicates began to incorporate more Mg²⁺ and Si⁴⁺ at temperatures ≥ 150 C°, this would release Fe²⁺ and Fe³⁺, necessitating the precipitation of another Fe-rich mineral such as magnetite (Figs. 4; 5d-5f; 9m). This process is described by Reaction 2, shown below:



Reaction 2 provides a clear pathway for the concurrent decrease of ferric iron in the silicate, decrease in pH, and increase in magnetite with temperature. Coincident with Fe

exsolution in the silicate, there was isomorphic substitution of Mg into the greenalite structure at higher temperatures (Fig. 12). While the ferric iron in magnetite could come from dissolved sources, our unchanging Fe(III)/FeT of the bulk precipitates and the temperature-induced shift from a more ferric silicate closer to cronstedtite to a more ferrous and magnesian greenalite-like iron silicate suggests that the Fe(III) in the higher-temperature magnetite derives from ferric iron exsolution in the lower-temperature iron silicates.

Implications

Our results reaffirm prior experimental studies that iron silicates require an elevated pH > 7 to precipitate under strictly ferrous conditions at low temperature (Hinz et al. 2021; Tosca et al. 2016). Reassuringly, we are continuing to validate these previous determinations under similar ferruginous and silica-rich conditions.

This work demonstrates that iron phyllosilicates will precipitate under simulated Archean ocean conditions as a result of in situ Fe(II) oxidation. We showed that in situ Fe(II) oxidation in the presence of silica at pH 7 can precipitate homogenous proto iron-rich phyllosilicates with a very low Mg content at 25 °C. At 80 °C, these precipitates crystallized into low-Mg iron phyllosilicates in the solid solution between greenalite and cronstedtite. These 80 °C iron silicate nanoparticles appeared remarkably similar to inclusions in early-forming BIF chert that are composed of low-Fe(III) greenalite with negligible Mg (Rasmussen et al. 2019; Johnson et al. 2018). With increasing temperatures simulating further diagenesis, these phyllosilicates transformed into a more greenalite-like mineral with less Fe(III) but considerably more Mg. The low (< 0.5 at.%) Mg content of iron phyllosilicate inclusions in BIF cherts suggests that they were likely formed under low temperatures, preserved and isolated in chert, restricting further reaction with Mg-containing seawater.

In the context of the BIF rock record, our observations could also provide insights into how diagenesis in the presence of Mg-rich fluids affects the crystallization and transformation of other BIF iron silicates as well. Broader scale BIF studies of iron silicates (greenalite, minnesotaite, and stilpnomelane) that are not preserved in chert can have a large range of Mg content (0.6-6.7 weight% MgO) within the silicate phases (Klein 2005; Klein 1974; Floran and Papike 1978). Our data would suggest the more elevated (> ~2 at.%) levels of Mg in these silicates derived from continued higher-temperature alteration of the initial BIF sediments, without the isolation provided by early-mineralizing chert. Consistent with this idea, observations of the silicate-bearing facies collected from separate localities with different degrees of BIF diagenesis were measured to have different Fe:Mg ratios (Floran and Papike 1978).

The formation of magnetite that we observed after the simulated diagenesis of iron silicates at high temperatures of ≥ 150 °C illuminates how BIF sediments may be expected to transform into secondary minerals. Magnetite is ubiquitous in BIF facies, but its origin is not well understood (Klein 2005). Previous petrographic studies of BIFs have shown that most, if not all, of the magnetite in these formations is a relatively late-formed mineral (Goodwin 1956; Laberge 1964; French, 1968, 1973; Han 1982; Kaufman et al. 1990; Kaufman 1996; Beukes and

Gutzmer 2008; Rasmussen and Muhling 2018). Intriguingly, petrographic observations support magnetite replacing early iron silicate granules (French 1968; Klein 1974; Floran and Papike 1978; Rasmussen and Muhling, 2018). Our results demonstrated that the simulated diagenesis of Fe(II,III) silicates at ≥ 80 °C indeed produces magnetite (Fig. 12b-12d), directly providing experimental evidence for petrographic observations of iron silicates altering to magnetite during diagenesis. Magnetite in BIF deposits thus represents diagenesis and/or post depositional alteration, obscuring the primary mineral(s) from which the magnetite derived. However, our experiments suggest that iron-rich silicate phases are a highly plausible precursor to BIF magnetite.

Our simulated diagenesis experiments therefore demonstrate the effects of diagenesis on iron silicates, with clear changes to the Fe(III) content and Mg content, and ultimately provide both an explanation for the origin of magnetite and guidance on how to interpret the magnesium content in iron-rich silicates in the BIF record.

Acknowledgements

I foremost thank Jena Johnson (University of Michigan, Michigan, USA) for her continued dedication, patience, and countless revisions—without your help, this work would not have been possible. I especially thank David Diercks (Colorado School of Mines, Golden, Colorado, USA) for assistance with TEM imaging and analyses. I thank Chi Ma (California Institute of Technology, Pasadena, California, USA) for assisting with TEM phase characterization and Victoria Jarvis (McMaster University, Hamilton, Ontario, Canada) for performing the Co-XRD measurements. I acknowledge funding from NASA Exobiology (J.E.J., Award #80NSSC18K1060) and NSF Geobiology and Low-Temperature Geochemistry (J.E.J., Award # 2142509) that supported this work.

References

- Baldermann, A., Dohrmann, R., Kaufhold, S., Nickel, C., Letofsky-Papst, I., and Dietzel, M. (2014) The Fe-Mg-saponite solid solution series – a hydrothermal synthesis study. *Clay Minerals*, 49, 391–415.
- Beard, J.S., Frost, R.B., Fryer, P., McCaig, A., Searle, R., Ildefonse, B., Zinin, P., and Sharma, S.K. (2009) Onset and Progression of Serpentinization and Magnetite Formation in Olivine-rich Troctolite from IODP Hole U1309D. *Journal of Petrology*, 50, 387-403.
- Beard, J.S., and Frost, R.B. (2017) The stoichiometric effects of ferric iron substitutions in serpentine from microprobe data. *International Geology Review*, 59, 5-6.
- Bekker, A., Slack, J.F., Planavsky, N., Krapez, B., Hofmann, A., Konhauser, K.O., and Rouxel, O.J. (2010) Iron Formation: The Sedimentary Product of a Complex Interplay among Mantle, Tectonic, Oceanic, and Biospheric Processes. *Economic Geology*, 105, 467–508.
- Bekker, A., Planavsky, N.J., Krapež, B., Rasmussen, B., Hofmann, A., Slack, J.F., Rouxel, O.J., and Konhauser, K.O. (2014) Iron Formations: Their Origins and Implications for Ancient Seawater Chemistry. In *Treatise on Geochemistry* pp. 561–628. Elsevier.

- Beukes, N.J. (1984) Sedimentology of the Kuruman and Griquatown Iron-formations, Transvaal Supergroup, Griqualand West, South Africa. *Precambrian Research*, 24, 47–84.
- Beukes, N.J., and Gutzmer, J. (2008) Origin and Paleoenvironmental Significance of Major Iron Formations at the Archean-Paleoproterozoic Boundary. In *Banded Iron Formation-Related High-Grade Iron Ore*. Society of Economic Geologists.
- Blättler, C.L., and Higgins, J.A. (2017) Testing Urey's carbonate–silicate cycle using the calcium isotopic composition of sedimentary carbonates. *Earth and Planetary Science Letters*, 479, 241–251.
- Bowes, D.R., and Farrow, C.M. (1997) Major and trace element compositions of the UICC standard asbestos samples. *American Journal of Industrial Medicine*, 32, 592–594.
- Braterman, P.S., Cairns-Smith, A.G., and Sloper, R.W. (1983) Photo-oxidation of hydrated Fe²⁺ significance for banded iron formations. *Nature*, 303, 163–164.
- Brenner, R.L., Ludvigson, G.A, Scal, R., and Dogen, A.U. (1991) Digenetic modeling of siliciclastic systems; status report. *Kansas State Geological Survey*, 233, 123-137.
- Buchholz, A., Laskov, C., and Haderlein, S.B. (2011) Effects of Zwitterionic Buffers on Sorption of Ferrous Iron at Goethite and Its Oxidation by CCl₄. *Environmental Science & Technology*, 45, 3355–3360.
- Burton, E.D., Bush, R.T., Sullivan, L.A., and Mitchell, D.R.G. (2007) Reductive transformation of iron and sulfur in schwertmannite-rich accumulations associated with acidified coastal lowlands. *Geochimica et Cosmochimica Acta*, 71, 4456–4473.
- Cairns-Smith, A.G. (1978) Precambrian solution photochemistry, inverse segregation, and banded iron formations. *Nature*, 276, 807–808.
- Capitani, G., and Mellini, M. (2004) The modulated crystal structure of antigorite: The m = 17 polysome. *American Mineralogist*, 89, 147-158.
- Caruso, L.J., and Chernosky, J.V. (1979) The Stability of Lizardite. *Canadian Mineralogist*, 17, 757-769.
- Cloud, P. (1973) Paleocological Significance of the Banded Iron-Formation. *Economic Geology*, 68, 1135–1143.
- Cornell, R.M., and Schwertmann, U. (2003) *The Iron Oxides: Structure, Properties, Reactions, Occurrences and Uses*, 1st ed. Wiley.
- D19 Committee (2016) D859-16 Test Method for Silica in Water. ASTM International.
- Derry, L.A. (2015) Causes and consequences of mid-Proterozoic anoxia: CAUSES OF MID-PROTEROZOIC ANOXIA. *Geophysical Research Letters*, 42, 8538–8546.

- Derry, L.A., and Jacobsen, S.B. (1990) The chemical evolution of Precambrian seawater: Evidence from REEs in banded iron formations. *Geochimica et Cosmochimica Acta*, 54, 2965–2977.
- Dietzel, M. (2000) Dissolution of silicates and the stability of polysilicic acid. *Geochimica et Cosmochimica Acta*, 64, 3275–3281.
- Doelsch, E., Rose, J., Masion, A., Bottero, J.Y., Nahon, D., and Bertsch, P.M. (2002) Hydrolysis of Iron(II) Chloride under Anoxic Conditions and Influence of SiO_4 Ligands. *Langmuir*, 18, 4292–4299.
- Evans, B.W. (2008) Control of the products of serpentinization by $\text{Fe}^{2+}\text{Mg}_{-1}$ exchange potential of olivine and orthopyroxene. *Journal of petrology*, 49, 1873-1887.
- Falini, G., Foresti, E., Gazzano, M., Gualtieri, A.F., Leoni, M., Lesci, I.G., and Roveri, N. (2004) Tubular-Shaped Stoichiometric Chrysotile Nanocrystals. *Chemistry - A European Journal*, 10, 3043–3049.
- Farmer, V.C., Krishnamurti G.S.R., and Huang, P.M. (1991) Synthetic allophane and layer-silicate formation in $\text{SiO}_2\text{-Al}_2\text{O}_3\text{-FeO-Fe}_2\text{O}_3\text{-MgO}$ systems at 23C and 89C in a calcareous environment. *Clays Clay Mineralogy*, 36, 561-570.
- Farquhar, J., Zerkle, A.L., and Bekker, A. (2011) Geological constraints on the origin of oxygenic photosynthesis. *Photosynthesis Research*, 107, 11–36.
- Fischer, W.W., and Knoll, A.H. (2009) An iron shuttle for deepwater silica in Late Archean and early Paleoproterozoic iron formation. *Geological Society of America Bulletin*, 121, 222-235.
- Floran, R.J., and Papike, J.J. (1978) Mineralogy and Petrology of the Gunflint Iron Formation, Minnesota-Ontario: Correlation of Compositional and Assemblage Variations at Low to Moderate Grade. *Journal of Petrology*, 19, 215–288.
- Francisco, P.C.M., Mitsui, S., Ishidera, T., Tachi, Y., Doi, R., and Shiwaku, H. (2020) Interaction of FeII and Si under anoxic and reducing conditions: Structural characteristics of ferrous silicate co-precipitates. *Geochimica et Cosmochimica Acta*, 270, 1–20.
- French, B.M. (1968) Progressive contact metamorphism of the Biwabik Iron Formation, Mesabi Range, Minnesota. *Minnesota Geologic Survey*, 64,103.
- French, B.M. (1973) Mineral Assemblages in Diagenetic and Low-Grade Metamorphic Iron-Formation. *Economic Geology*, 68, 1063–1074.
- Fuchs, Y., Linares, J., and Mellini, M. (1998) Mossbauer and infrared spectrometry of lizardite-1T from Monte Fico, Elba. *Physical Chemical Minerals*, 26, 111-115.
- Goodwin, A.M. (1956) Facies relations in the Gunflint iron formation [Ontario]. *Economic Geology*, 51, 565–595.

- Guggenheim, S., and Bailey, S.W. (1989) An occurrence of a modulated serpentine related to the greenalite-caryopilite series. *American Mineralogist*, 74, 637-641.
- Guggenheim, S., Bailey, S.W., Eggleton, R.A., and Wilkes, P. (1982). Structural aspects of greenalite and related minerals. *Canadian Mineralogist*, 20, 1-18.
- Guggenheim, S., and Eggleton, R.A. (1998) Modulated crystal structures of greenalite and caryopilite: a system with a long range, in-plane structural disorder in the tetrahedral sheet. *Canadian Mineralogist*, 36, 163-179.
- Gumsley, A.P., Chamberlain, K.R., Bleeker, W., Söderlund, U., de Kock, M.O., Larsson, E.R., and Bekker, A. (2017) Timing and tempo of the Great Oxidation Event. *Proceedings of the National Academy of Sciences*, 114, 1811–1816.
- Gunnarsson, I., and Arnórsson, S. (2000) Amorphous silica solubility and the thermodynamic properties of H_4SiO_4 in the range of 0° to 350°C at Psat. *Geochimica et Cosmochimica Acta*, 64, 2295–2307.
- Haavik, C., Stølen, S., Fjellvåg, H., Hanfland, M., and Häusermann, D. (2000) Equation of state of magnetite and its high-pressure modification: Thermodynamics of the Fe-O system at high pressure. *American Mineralogist*, 85, 514–523.
- Halevy, I., and Bachan, A. (2017) The geologic history of seawater pH. *Science*, 355, 1069–1071.
- Han, T.M. (1982) Iron Formations of Precambrian Age: Hematite-Magnetite Relationships in Some Proterozoic Iron Deposits - A Microscopic Observation. *Ore Genesis*.
- Hansel, C.M., Benner, S.G., and Fendorf, S. (2005) Competing Fe(II)-Induced Mineralization Pathways of Ferrihydrite. *Environmental Science & Technology*, 39, 7147–7153.
- Hartman, H. (1984) The evolution of photosynthesis and microbial mats: A speculation on the banded iron formations. In Cohen, Y., Castenholz, R.W., and Halvorson, H.O. *Microbial Mats: Stromatolites*. Alan R Liss, 449-453.
- Hinz, I.L., Nims, C., Theuer, S., Templeton, A.S., and Johnson, J.E. (2021) Ferric iron triggers greenalite formation in simulated Archean seawater. *Geology*, 49, 905–910.
- Holland, H.D. (1984) *The Chemical Evolution of the Atmosphere and Oceans*. Princeton University Press, 598.
- Hostetler, P.B., and Christ, C.L. (1968) Studies in the system $\text{MgO-SiO}_2\text{-CO}_2\text{-H}_2\text{O(l)}$: The activity-product constant of chrysotile. *Geochimica et Cosmochimica Acta*, 32, 485-497.
- Howard, K.T., Benedix, G.K., Bland, P.A., and Cressey, G. (2011) Modal mineralogy of CM chondrites by X-ray diffraction (PSD-XRD): Part 2. Degree, nature and settings of aqueous alteration. *Geochimica et Cosmochimica Acta*, 75, 2735-2751.

- Hybler, J., Petricek, A., Durovic, I.S., and Smrcok, L. (2000) REFINEMENT OF THE CRYSTAL STRUCTURE OF CRONSTEDTITE-IT. *Clays and Clay Minerals*, 8.
- Isson, T.T., and Planavsky, N.J. (2018) Reverse weathering as a long-term stabilizer of marine pH and planetary climate. *Nature*, 560, 471–475.
- Izawa, M.R.M., Nesbitt, H.W., MacRae, N.D., and Hoffman, E.L. (2010) Composition and evolution of the early oceans: Evidence from the Tagish Lake meteorite. *Earth and Planetary Science Letters*, 298, 443–449.
- James, H.L. (1954) Sedimentary Facies of Iron-Formation. *Economic Geology*, 49, 235-293.
- Janecky, D.R., and Seyfried, W.E. (1986) Hydrothermal serpentinization of peridotite within the ocean crust: Experimental investigations of mineralogy and major element chemistry. *Geochimica et Cosmochimica Acta*, 50, 1357-1378.
- Jiang, C.Z., and Tosca, N.J. (2019) Fe(II)-carbonate precipitation kinetics and the chemistry of anoxic ferruginous seawater. *Earth and Planetary Science Letters*, 506, 231–242.
- Johnson, J.E., and Molnar, P.H. (2019) Widespread and Persistent Deposition of Iron Formations for Two Billion Years. *Geophysical Research Letters*, 46, 3327–3339.
- Johnson, J.E., Muhling, J.R., Cosmidis, J., Rasmussen, B., and Templeton, A.S. (2018) Low-Fe(III) Greenalite Was a Primary Mineral From Neoproterozoic Oceans. *Geophysical Research Letters*, 45, 3182–3192.
- Jones, C., Nomosatryo, S., Crowe, S.A., Bjerrum, C.J., and Canfield, D.E. (2015) Iron oxides, divalent cations, silica, and the early earth phosphorus crisis. *Geology*, 43, 135–138.
- Kappler, A., Pasquero, C., Konhauser, K.O., and Newman, D.K. (2005) Deposition of banded iron formations by anoxygenic phototrophic Fe(II)-oxidizing bacteria. *Geology*, 33, 865.
- Kaufman, A.J. (1996) Geochemical and mineralogic effects of contact metamorphism on banded iron-formation: an example from the Transvaal Basin, South Africa. *Precambrian Research*, 79, 171–194.
- Kaufman, A.J., Hayes, J.M., and Klein, C. (1990) Primary and diagenetic controls of isotopic compositions of iron-formation carbonates. *Geochimica et Cosmochimica Acta*, 54, 3461–3473.
- Keeling, J.L., Raven, M.D., and Self, P.G. (2010). Asbestiform antigorite-implications for the risk assessment of fibrous silicates. 21st Australian Clay Minerals Conference.
- Kinsela, A.S., Jones, A.M., Bligh, M.W., Pham, A.N., Collins, R.N., Harrison, J.J., Wilsher, K.L., Payne, T.E., and Waite, T.D. (2016) Influence of Dissolved Silicate on Rates of Fe(II) Oxidation. *Environmental Science & Technology*, 50, 11663–11671.
- Klein, C. (1974) Greenalite, Stilpnomenlane, Minnesotaite, Crocidolite and Carbonates in a very

- Low-Grade Metamorphic Precambrian Iron-Formation. *Canadian Mineralogist*, 12, 475-498.
- Klein, C. (2005) Some Precambrian banded iron-formations (BIFs) from around the world: Their age, geologic setting, mineralogy, metamorphism, geochemistry, and origins. *American Mineralogist*, 90, 1473–1499.
- Klein, F., Back, W., Jons, N., McCollom, T., Moskowitz, B., and Berquo, T. (2009) Iron partitioning and hydrogen generation during serpentinization of abyssal peridotites from 15°N on the Mid-Atlantic Ridge. *Geochimica et Cosmochimica Acta*, 73, 6868-6893.
- Klein, C., and Beukes, N.J. (1989) Geochemistry and sedimentology of a facies transition from limestone to iron-formation deposition in the early Proterozoic Transvaal Supergroup, South Africa. *Economic Geology*, 84, 1733–1774.
- Klein, C., and Beukes, N.J. (1992) Models for iron-formation deposition. Cambridge University Press, 147-151.
- Konhauser, K.O., Hamade, T., Raiswell, R., Morris, R.C., Grant Ferris, F., Southam, G., and Canfield, D.E. (2002) Could bacteria have formed the Precambrian banded iron formations? *Geology*, 30, 1079.
- Konhauser, K.O., Planavsky, N.J., Hardisty, D.S., Robbins, L.J., Warchola, T.J., Haugaard, R., Lalonde, S.V., Partin, C.A., Oonk, P.B.H., Tsikos, H., and others (2017) Iron formations: A global record of Neoarchaeon to Palaeoproterozoic environmental history. *Earth-Science Reviews*, 172, 140–177.
- Krissansen-Totton, J., Arney, G.N., and Catling, D.C. (2018) Constraining the climate and ocean pH of the early Earth with a geological carbon cycle model. *Proceedings of the National Academy of Sciences*, 115, 4105–4110.
- LaBerge, G.L. (1964) Development of Magnetite in Iron-Formations of the Lake Superior Region. *Economic Geology*, 59, 1313-1342.
- Lafuente, B., Downs, R.T., Yang, H., Stone, N. (2015). The power of databases: the RRUFF project. *Highlights in Mineralogical Crystallography*, 1-30.
- Maliva, R.G., Knoll, A.H., and Simonson, B.M. (2005) Secular change in the Precambrian silica cycle: Insights from chert petrology. *Geological Society of America Bulletin*, 117, 835.
- McSween, H.Y. (1979) Are Carbonaceous Chondrites Primitive or Processed? A Review. *Reviews of Geophysics and Space Physics*, 17, 1059-1078.
- Mizutani, T. (1991) Synthesis of 1:1 and 2:1 Iron Phyllosilicates and Characterization of their Iron State by Mössbauer Spectroscopy. *Clays and Clay Minerals*, 39, 381–386.
- Muhling, J.R., and Rasmussen, B. (2020) Widespread deposition of greenalite to form Banded Iron Formations before the Great Oxidation Event. *Precambrian Research*, 339, 105619.

- Nitschmann, H. (1938) Reaktionslenkung durch Keime. Beobachtungen bei der Oxydation von Eisen in Eisen(II)-sulfatlösung. *Helvetica Chimica Acta*, 21, 1609–1618.
- O’Hanley, D.S. (1996) *Serpentinites: Records of Tectonic and Petrologic History*, Oxford University Press, 78, 137-138.
- O’Hanley, D.S., and Dyar, M.D. (1993) The composition of lizardite 1T and the formation of magnetite in serpentinites. *American Mineralogist*, 78, 391-404.
- O’Hanley, D.S., and Dyar, M.D. (1998) The composition of chrysotile and its relationship with lizardite. *The Canadian Mineralogist*, 36, 727-739.
- Pavlov, A.A., and Kasting, J.F. (2002) Mass-Independent Fractionation of Sulfur Isotopes in Archean Sediments: Strong Evidence for an Anoxic Archean Atmosphere. *Astrobiology*, 2, 27–41.
- Pecharrromfin, C., Gonzfilez-Carrefio, T., and Iglesias, J.E. (1995) The Infrared Dielectric Properties of Maghemite, $\gamma\text{-Fe}_2\text{O}_3$, from Reflectance Measurement on Pressed Powders. *Physical Chemical Minerals*, 22, 21-29.
- Pedersen, H.D., Postma, D., Jakobsen, R., and Larsen, O. (2005) Fast transformation of iron oxyhydroxides by the catalytic action of aqueous Fe(II). *Geochimica et Cosmochimica Acta*, 69, 3967–3977.
- Persson, I. (2018) Ferric Chloride Complexes in Aqueous Solution: An EXAFS Study. *Journal of Solution Chemistry*, 47, 797–805.
- Philippini, V., Naveau, A., Catalette, H., and Leclercq, S. (2006) Sorption of silicon of magnetite and other corrosion products of iron. *Journal of Nuclear Materials*, 348, 60-69.
- Pignatelli, I., Mugnoili, E., Hybler, J., Mosser-Ruck, R., Cathelineau, M., and Michau, N. (2013) A multi-technique characterization of cronstedtite synthesized by iron-clay interaction in a step-by-step cooling procedure. *Clays and Clay Minerals*, 61, 277-289.
- Pignatelli, I., Bourdelle, F., Bartier, D., Mosser-Ruck, R., Truche, L., Mugnaioli, E., and Michau, N. (2014) Iron-clay interactions: Detailed study of the mineralogical transformation of claystone with emphasis on the formation of iron-rich T-O phyllosilicates in a step-by-step cooling experiment from 90 °C to 40 °C. *Chemical Geology*, 387, 1-11.
- Postma, D. (1993) The reactivity of iron oxides in sediments: A kinetic approach. *Geochimica et Cosmochimica Acta*, 57, 5027–5034.
- Poulton, S.W., Bekker, A., Cumming, V.M., Zerkle, A.L., Canfield, D.E., and Johnston, D.T. (2021) A 200-million-year delay in permanent atmospheric oxygenation. *Nature*, 592, 232–236.
- Rasmussen, B., and Muhling, J.R. (2018) Making magnetite late again: Evidence for widespread magnetite growth by thermal decomposition of siderite in Hamersley banded iron

- formations. *Precambrian Research*, 306, 64–93.
- Rasmussen, B., Krapež, B., and Muhling, J.R. (2015) Seafloor silicification and hardground development during deposition of 2.5 Ga banded iron formations. *Geology*, 43, 235–238.
- Rasmussen, B., Muhling, J.R., Tosca, N.J., and Tsikos, H. (2019) Evidence for anoxic shallow oceans at 2.45 Ga: Implications for the rise of oxygenic photosynthesis. *Geology*, 47, 622–626.
- Rasmussen, B., Muhling, J.R., and Fischer, W.W. (2021) Greenalite Nanoparticles in Alkaline Vent Plumes as Templates for the Origin of Life. *Astrobiology*, 21, 246–259.
- Riley, J.P. and Chester, R. (1971) *Introduction to marine chemistry*. Academic Press, London.
- Sayles, F.L. and Fyfe, W.S. (1973) The crystallization of magnesite from aqueous solution. *Geochimica et Cosmochimica Acta*, 37, 87-99.
- Shervais, J.W., Kolesar, P., and Andreasen, K. (2005) A Field and Chemical Study of Serpentinization-Stonyford, California: Chemical Flux and Mass Balance. *International Geology Review*, 47, 1-23.
- Siever, R. (1986) Burial Diagenesis of Sandstones. *U.S. Geological Survey Bulletin*, 1578, 237-248.
- Siever, R. (1992) The silica cycle in the Precambrian. *Geochimica et Cosmochimica Acta*, 56, 3265–3272.
- Spencer, R.J. and Hardie, L.A. (1990) Control of seawater composition by mixing of river waters and mid-ocean ridge hydrothermal brines. *The Geochemical Society*, 2, 409-419.
- Stefánsson, A. (2007) Iron(III) Hydrolysis and Solubility at 25 °C. *Environmental Science & Technology*, 41, 6117–6123.
- Stefurak, E.J.T., Lowe, D.R., Zentner, D., and Fischer, W.W. (2015) Sedimentology and geochemistry of Archean silica granules. *Geological Society of America Bulletin*, B31181.1.
- Stookey, L.L. (1970) Ferrozine---a new spectrophotometric reagent for iron. *Analytical Chemistry*, 42, 779–781.
- Stüeken, E.E., Kipp, M.A., Koehler, M.C., and Buick, R. (2016) The evolution of Earth's biogeochemical nitrogen cycle. *Earth-Science Reviews*, 160, 220–239.
- Sun, S., Konhauser, K.O., Kappler, A., and Li, Y.-L. (2015) Primary hematite in Neoproterozoic to Paleoproterozoic oceans. *Geological Society of America Bulletin*, 127, 850–861.
- Suttle, M.D., King, A.J., Schofield, P.F., and Russell, S.S. (2021) The aqueous alteration of CM chondrites, a review. *Geochimica et Cosmochimica Acta*, 299, 219-256.

- Tomeoka, K., McSween, H.Y., and Buseck, P.R. (1989) Mineralogical Alteration of CM Carbonaceous Chondrites: A Review. *Proceedings of the NIPR Symposium on Antarctic Meteorites*, 2, 221-234.
- Tosca, N.J., Macdonald, F.A., Strauss, J.V., Johnston, D.T., and Knoll, A.H. (2011) Sedimentary talc in Neoproterozoic carbonate successions. *Earth and Planetary Science Letters*, 306, 11–22.
- Tosca, N.J., Guggenheim, S., and Pufahl, P.K. (2016) An authigenic origin for Precambrian greenalite: Implications for iron formation and the chemistry of ancient seawater. *Geological Society of America Bulletin*, 128, 511–530.
- Tosca, N.J., Ahmed, I.A.M., Tutolo, B.M., Ashpitel, A., and Hurowitz, J.A. (2018) Magnetite authigenesis and the warming of early Mars. *Nature Geoscience*, 11, 635–639.
- Trendall, A.F. (2002) The Significance of Iron-Formation in the Precambrian Stratigraphic Record. In W. Altermann and P.L. Corcoran, Eds., *Precambrian Sedimentary Environments* pp. 33–66. Blackwell Publishing Ltd., Oxford, UK.
- Trittschack, R., Grobety, B., and Brodard, P. (2014) Kinetics of the chrysotile and brucite dehydroxylation reaction: a combined non-isothermal/isothermal thermogravimetric analysis and high-temperature X-ray powder diffraction study. *Physics and Chemistry of Minerals*, 41, 197-214.
- Tutolo, B.M., Evans, B.W., and Kuehner, S.M. (2019) Serpentine-Hisingerite Solid Solution in Altered Ferroan Peridotite and Olivine Gabbro. *Minerals*, 47, 1-14.
- Vacher, L.G., Truche, L., Faure, F., Tissandier, L., Mosser-Ruck, R., and Marrocchi, Y. (2019) Deciphering the conditions of tochilinite and cronstedtite formation in CM chondrites from low temperature hydrothermal experiments. *Meteoritics & Planetary Science*, 54, 1870–1889.
- Velde, B. (2003) Green Clay Minerals. *Treatise on Geochemistry*, 7, 309-324.
- Viollier, E., Inglett, P.W., Hunter, K., Roychoudhury, A.N., and Van Cappellen, P. (2000) The ferrozine method revisited: Fe(II)/Fe(III) determination in natural waters. *Applied Geochemistry*, 15, 785–790.
- Votyakov, S.L., Chashchukhin, O.L., Galakhova, O.L., and Gulyaeva, T. Y. (2005) Crystal Chemistry of Lizardite as an Indicator of Early Serpentinization in Ultramafic Rocks I. Compositional and Structural Features of the Mineral According to Spectroscopic Data. *Geochemistry International*, 43, 862-880.
- Walter, M., Schenkeveld, W.D.C., Reissner, M., Gille, L., and Kraemer, S.M. (2019) The Effect of pH and Biogenic Ligands on the Weathering of Chrysotile Asbestos: The Pivotal Role of Tetrahedral Fe in Dissolution Kinetics and Radical Formation. *Chemistry – A European Journal*, 25, 3286–3300.

Wicks, F.J., and O'Hanley, D.S. (2018) Chapter 5. Serpentine Minerals: Structures and Petrology. *Hydrous Phyllosilicates*, 91-168.

Zolotov, M.Y. (2014) Formation of brucite and cronstedtite-bearing mineral assemblages on Ceres. *Icarus*, 228, 13–26.

Table & Figure Captions

Table 1. Composition of recreated Archean seawater. Iron and silica concentrations shown as measured concentrations derived from colorimetric (ferrozine and silicomolybdate) assays where * denotes the standard deviation of the measurement.

Table 2: Measured pH for each experiment during the O₂ bubbling process at 25 °C where solutions were adjusted by anoxic 2 M hydrochloric acid to hold the pH around 7. Note: the error for each pH measurement was ± 0.02 pH units.

Table 3. pH measurements of Parr vessel precipitates and overlaying solution for control and bubbled experiments for temperatures that ranged from 25-220 °C. Note: pH measurements were taken after the solution was cooled to 25 °C to minimize temperature compensation and the error for each pH measurement was ± 0.02 pH units.

Table 4: Summary of experimental results of Fe(II) and silica in initial solutions. The measured Fe[III]/FeT content for the acidified control and bubbled experiments (solution plus precipitate) after aging in a borosilicate bottle at 25 °C for 19 days.

Table 5. The measured Fe[III]/FeT content of the acidified control and bubbled solid precipitate from conditions ranging 25-220 °C over 19-40 total days.

Table 6. Summary of the average elemental composition of the phases (in atomic % or as a ratio) at each experimental condition.

Figure 1: Time-temperature scheme for hydrothermal aging of control and bubbled experiments. The reaction with O₂ and equilibrium period took place in borosilicate bottles denoted by the light gray region. Control and bubbled experiments were subsampled for pH (Table 3) and Fe(III)/FeT (Table 4) after 19 days at room temperature (star symbol). The remainder of material

was portioned and transferred into anoxic Parr vessels for aging at 25, 80, 150, and 220 °C before being sampled (filled circles, Table 5).

Figure 2. Plot of pH measurements from Parr vessel with precipitate and overlaying solution for control and bubbled experiments for temperatures that ranged from 25 - 220 °C. Note the uncertainty of the pH measurements and oven temperatures was ± 0.02 pH units and ± 0.4 °C respectively.

Figure 3. The measured Fe(III)/FeT content of the acidified control precipitates and bubbled precipitates along with the calculated standard deviation from replicate measurements.

Figure 4: Cobalt sourced XRD patterns from replicate bubbled experimental precipitates subject to simulated diagenesis at 25 °C (Blue), 80 °C (Green), 150 °C (Black), and 220 °C (Red). Plotted for comparison: blank kapton tube (K); 1:1 iron-silicates greenalite (G), $[\text{Fe}^{2+}_3\text{Si}_2\text{O}_5(\text{OH})_4]$ (from Guggenheim et al. 1982) and cronstedtite (C), $[(\text{Fe}^{2+}, \text{Fe}^{3+})_3(\text{Si}, \text{Fe}^{3+})_2\text{O}_5(\text{OH})_4]$ (Lab Standard, Caltech Mineralogical Collection); and a spinel group iron-oxide, magnetite (M), $[\text{Fe}^{2+}\text{Fe}^{3+}_2\text{O}_4]$ (from Haavik et al. 2000). Both the copper and cobalt two theta axes are plotted for comparison. The experimental and standard diffraction patterns were vertically offset for clarity.

Figure 5: The precipitate from the 150 °C control experiment had a tan color (**a-left**) and was moderately attracted to the magnet (**a-right**). The precipitate from the 220 °C control experiment continued to have a tan color (**b-left**) but only some particles appeared to be attracted to the magnet (**b-right**). The precipitate from the bubbled experiment after aging at 25 °C had a green color (**c-top**) and was not attracted to the magnet (**c-bottom**). The bubbled experiment harvested after aging at 80 °C was green (**d-top**) and was moderately attracted to the magnet (**d-bottom**). The bubbled 150 °C precipitate was dark green (**e-top**) and continued to be moderately attracted to the magnet (**e-bottom**). The bubbled 220 °C precipitate was darker green (**f-top**) and was highly attracted to the magnet (**f-bottom**).

Figure 6: Tan precipitate harvested from control experiment after 7 days at 150 °C (**a**). Clumps of heterogeneous particles included: poorly formed tubular spindles (**b-c**) with a 2.3 Å (**d**) and 2.5 Å (**d-i**) lattice spacing; layered structures with frayed edges (**e**) where the two particles had 6.9 Å and 7.2 Å lattice spacings (**f**) and measured elemental chemistry (**g**; Table 6); blunt-edged rods (**h**) and the measured elemental chemistry (**i-j**; Table 6). Basal spacing of the blunt-edge rods was measured to be 6.2 Å (**k**), similar to another phase with a lathe-like morphology (**l**) and 3.2 Å and 6.1 Å lattice spacing (**l-i** & **l-ii**). The polynanocrystalline SAED pattern from a region containing blunt-edged rods and lathes was most consistent with lepidocrocite (**m**).

Figure 7: Tan precipitate harvested from control experiment after aging for 7 days at 220 °C (**a**). Homogenous clumps composed of hollow tubes (**b-d**) and measured elemental chemistry (**e**). Viewing down the tube axis and along the profile of the tube we measured the lattice spacing to be 7.2 Å in both instances (**f & g-i.**) and 4.3 Å at a separate orientation (**g-ii.**). A globular phase was observed (**h**) and elemental chemistry rich in Fe and O was mapped (**i**). SAED of a region containing both the tubular and globular phase respectively produced a polynanocrystalline pattern for a magnesium-silicate and planes for a spinel group, iron-oxide (**j**).

Figure 8: TEM-based observations of green precipitate (**a**) harvested from the bubbled experiment held at 25 °C for 40 days. Homogeneous distribution of particles with a spindly morphology (**b-f**) where the best captured particles exhibited a maximum of 3-4 layers (**d & f**) with an approximate basal spacing of ~7.2-7.7 Å determined by IFFT (**d-i., d-ii., f-i., & f-ii.**). SAED on a region of poorly layered particles produced diffuse rings corresponding to 1.3 Å, 1.5 Å, and 2.6 Å lattice spacings (**g**). HAADF image of poorly layered particles (**h-j**) with corresponding EDS maps of Fe, Si, and Mg (**h**); the average atomic values are reported in Table 6.

Figure 9: TEM analyses of green precipitate (**a**) harvested from bubbled experiment after 7 days at 80 °C. We observed a heterogeneous mixture of morphologies, including well-ordered blades (**b & c**) with the elemental chemistry maps shown for Fe, Si, Mg, and O (**d & e**, also see Table 6), containing a 7.2 Å lattice fringe (**f**); triangular-trapezoidal structures (**b-arrows, g, j, k**) showing Fe, Si, Mg, and O chemical maps (**h & i**). In this phase, the “caps” of the structure (**j**) had 7.0 Å and 3.1 Å (**j-i. & j-ii.**) while the “body” of the structure (**k**) had frequent crystal defects (**k-arrows**) and 7.2 Å lattice spacing (**k-i.**). SAED of a heterogeneous area similar to panel b produced recurring lattice planes (**l**). A third morphology observed were platelets that had a 4.7 Å lattice fringe (**m**) and multiple FFT lattice spacings corresponding to a spinel group phase such as magnetite (**m-i.**).

Figure 10: Observations of the dark green precipitate (**a**) harvested from a bubbled experiment after 7 days at 150 °C. TEM revealed a heterogeneous mixture of phases (**b**) containing well-ordered blades (**c-f**) where the lattice spacings were measured to be 7.2 Å (**d**) and 7.3 Å (**d-i.**). Some particles showed a basal lattice spacing (001) 7.1 Å (**f**) and 24 Å superlattice modulation (**f-i.**). We also observed a platelet phase with 4.7 Å lattice spacing (**g**) where FFT confirmed the presence of lattice planes consistent with a spinel group iron-oxide like magnetite (**g-i.**). The elemental chemistry of the layered blades indicated a phase rich in Fe and Si with a small amount of Mg (**h-j**; Table 6).

Figure 11: The bubbled experiment after 7 days at 220 °C yielded the darkest green precipitate (**a**). TEM revealed the heterogeneous phases (**b**) within this experiment that included well-ordered blades with a 7.1 Å lattice spacing (**c**) along with elemental chemistry rich in Fe, Si, and

Mg (**d**). An additional example of this layered, bladed phase (**e**) showed a 7.1 Å d-spacing (001) with superlattice modulation of 21 Å (**f & f-i.**), and elemental chemistry (**g**). Additionally, we observed a platelet phase with 4.7 Å lattice spacing (**h**) and FFT lattice planes consistent with a spinel group identification (**h-inset**); we also show the measured elemental chemistry of the platelet (**h-i.**). SAED of an area containing the platelets displayed polynanocrystalline halos at the lattice planes of a spinel group mineral (**j**).

Figure 12: Compilation of the layered phase observed in bubbled experiments at temperatures 25, 80, 150 and 220 °C. At 25 °C, we observed spindly particles (**a**) with a maximum of 4 layers (**a-i.**) measured with an approximate lattice spacing of 7.7 Å by IFFT (**a-ii.**) with FFT only showing the basal d-spacing (001) (**a-iii.**). Cluster of poorly layered particles in HAADF (**a-iv.**) and Mg distribution and content on average (**a-v.**). At 80 °C, we observed well-ordered particles (**b**) with extensive layering (**b-i.**) with a lattice fringe of 7.2 Å as measured by IFFT (**b-ii.**) and showing multiple lattice planes by FFT (**b-iii.**). Region with well ordered layered blades in HAADF (**b-iv.**) and Mg distribution and average content (**b-v.**). We observed similar well-ordered particles at 150 °C (**c**) with extensive layering (**c-i.**) where the lattice fringe was 7.1 Å by IFFT (**c-ii.**) and displayed recurring lattice planes by FFT (**c-iii.**). Collection of well-ordered particles in HAADF (**c-iv.**) alongside Mg distribution and content (**c-v.**). At 220 °C, we continued to observe a well-ordered layered phase (**d & d-i.**) with a measured lattice fringe of 7.1 Å by IFFT (**d-ii.**) and recurring lattice planes by FFT (**d-iii.**). Collection of well-ordered particles in HAADF (**d-iv.**) and Mg distribution and content (**d-v.**).